



Peridynamics for out-of-plane damage analysis of composite laminates

Xiongwu Yang¹ · Weicheng Gao¹ · Wei Liu¹ · Xiaole Li² · Fengshou Li¹

Received: 24 February 2023 / Accepted: 17 September 2023 / Published online: 12 October 2023
© The Author(s), under exclusive licence to Springer-Verlag London Ltd., part of Springer Nature 2023

Abstract

A new peridynamic model for predicting the out-of-plane bending and twisting behavior of composite laminates has been proposed, in which fiber bonds and matrix bonds are distinguished for characterizing anisotropy. The peridynamic formulations are obtained based on the principle of virtual displacements using the Total Lagrange formulation, and the equation of motion is reformulated by the interpolation technique. The critical curvature is adopted as the failure criterion, and a micromodulus reduction method is implemented in the PD algorithm. For multi-layer laminated structures, a new single-layer material point model (SLMPM) is proposed, in which the overall micromodulus is integrated according to all plies in laminates. The capability of the developed PD model was demonstrated by the bending examples of composite laminates with different fiber orientations, and damage analysis was further conducted to demonstrate the strong capability of the proposed PD model in replicating the failure process of composite structures. In addition, the computational efficiency of numerical models can be greatly improved due to the SLMPM.

Keywords Peridynamics · Damage · Laminate · Single-layer · Micromodulus reduction

1 Introduction

Fiber-reinforced composite materials are widely used in advanced aircraft, marine, automobile, and many other industries due to their excellent mechanical properties, i.e., the high stiffness-to-weight and strength-to-weight ratios, and corrosion resistance. Accurate prediction of progressive failure processes of composite structures is still an active and persistent challenge that requires much effort, especially for crack branch and multiple-crack problems. Since the partial-differential equations are invalid in the presence of discontinuities, there is a series of conceptual and mathematical difficulties in dealing with crack nucleation and propagation in the classical continuum mechanics (CCM). Peridynamics

(PD) is a reformulation of CCM [1–3] that can simulate the whole failure process of materials without additional failure criteria and stiffness degradation model, and continuous as well as discontinuous are described under the same theoretical framework. The great potential of the PD theory in capturing the damage pattern of laminated structures has been proved since its development [4, 5].

In the past decades, the peridynamic theory has been utilized successfully for failure analysis for various engineering problems, such as rock cracking [6–8], concrete structures damage [9–11], bimaterial damage [12–14], etc., which demonstrated the strong capability of peridynamics in capturing crack initiation and its propagation. However, most of the research objects are solid structures or simplified as two-dimensional plane problems. For a plate, shell, or slender structure, it is almost impossible to simulate the failure mode by the 3D PD model due to the extremely low computational efficiency. Therefore, structural idealization is essential to improve accuracy and efficiency, and the advantage can also be presented in other numerical techniques, such as finite element analysis [15–17]. In peridynamics, the first PD model for 2D configurations was introduced by Silling and Bobaru [18]. O’Grady and Foster [19] proposed a non-ordinary

✉ Weicheng Gao
gaoweicheng@sina.com

¹ Department of Astronautic Science and Mechanics, Harbin Institute of Technology, Harbin, People’s Republic of China

² Mechanics of Composites for Energy and Mobility Lab, Mechanical Engineering Program, Physical Science and Engineering Division, King Abdullah University of Science and Technology (KAUST), 23955-6900 Thuwal, Kingdom of Saudi Arabia

stated-based PD (NOSBPD) model for Kirchhoff–Love plate, in which a bond-pair model is used to describe the bending behavior; Diyaroglu et al. [20] developed a bond-based PD (BBPD) theory for Timoshenko beam and Mindlin plate, in which the transverse shear deformation is considered; Nguyen and Oterkus [21] derived an ordinary stated-based PD (OSBPD) theory using Total Lagrange formulation, and the thermomechanical behavior of shell structures can be simulated. Later, the geometrically nonlinear theory of plates and shells was also further developed by Nguyen and Oterkus [22, 23]. In addition, Shen et al. [24] developed a micro-beam bond model for plate structures.

The general PD model for laminates was established by Oterkus and Madenci [25]. The in-plane behavior of laminates is characterized by fiber bonds and matrix bonds, and the interlayer behavior is characterized by the interlayer normal bonds and shear bonds, namely the four bond-based model (FBBM). Owing to FBBM, some efforts have been made to apply it to study the damage problem of laminated composites subjected to quasi-static loads [26–29], impact loads [27], explosion loads [30, 31], etc. Furthermore, because the anisotropic properties of materials can also be described through the fourth-order elastic matrix [32, 33], different failure problems for laminated structures have also been studied successively by NOSBPD [34–38]. In addition, Hu et al. [39–41] developed a new BBPD model for composite laminates that can remove limitations of FBBM in Poisson's ratio and fiber orientation. Jiang et al. [42, 43] established an OSBPD model of laminates by replacing the cylindrical horizon with a spherical horizon. Guo et al. [44] and Braun et al. [45–48] derived the lattice-based PD models with different topological forms and successfully simulated the linear elastic deformation and damage pattern of FRP laminates. In addition, PD models for the microstructure of composite materials have also been proposed successively [49, 50].

Up to now, most PD theories only focused on the in-plane mechanical behavior of composite structures. The PD theory describing the out-of-plane bending and twisting behavior of composite materials is rarely studied. Although Tastan and Ugur [51, 52] proposed a PD model for anisotropic materials by introducing bending stiffness and angular displacements, only the unidirectional laminate can be simulated. Hu et al. [40] proposed a PD model based on Mindlin theories to account for material coupling and transverse shear

deformation, but the fiber and matrix damage of laminates cannot be well captured. In practical engineering, it is almost impossible to predict the damage pattern of composite structures only relying on the existing PD theory due to the complex load cases. Moreover, large composite structures with complex geometric configurations cannot be simulated due to the lack of out-of-plane theory, which will limit the engineering value of PD theory on real-scale composite structures. Therefore, it is still an urgent task to develop an out-of-plane PD theory for composite laminates.

In this paper, a new PD model for the out-of-plane mechanical behavior of composite laminates is developed, in which bending micromodulus are distinguished in different directions for characterizing anisotropy. The PD micropotentials for the Kirchhoff plate are achieved by interpolation technique, and the PD formulations and equations of motion are obtained based on the principle of virtual displacements using the Total Lagrange formulation. The critical curvature is adopted as the failure criterion, and the strength difference between the carbon fiber rod and resin matrix is described by different critical values. To model composite laminates, the interlaminar deformation compatibility assumption needs to be introduced in the proposed PD model. The overall micromodulus of laminates is integrated according to all plies, and the stiffness behavior is described by means of a micromodulus reduction method. Due to the assumption of interlaminar deformation compatibility, the mechanical behavior of multi-layer laminates can be simulated only by single-layer material points and, thus, the computational efficiency of numerical models is greatly improved.

The remainder of the paper is organized as follows. Section 2 presents the PD kinematics and the corresponding PD equations of motion for composite laminates. Critical curvature and micromodulus reduction method are provided in Sect. 3. An alternative numerical technique is provided in Sect. 4. Validation and demonstration of the PD model on deformation and damage examples are presented in Sect. 5. The paper is closed with conclusions and perspectives in Sect. 6.

2 Peridynamic equations of motion for composite laminates

In peridynamics, the motion of material points can be described using integrodifferential equations as:

$$\rho(\mathbf{x})\ddot{\mathbf{u}}(\mathbf{x}, t) = \int_{H_x} (\mathbf{t}(\mathbf{u}' - \mathbf{u}, \mathbf{x}' - \mathbf{x}, t) - \mathbf{t}'(\mathbf{u} - \mathbf{u}', \mathbf{x} - \mathbf{x}', t)) dV' + \mathbf{b}(\mathbf{x}, t) \quad (1)$$

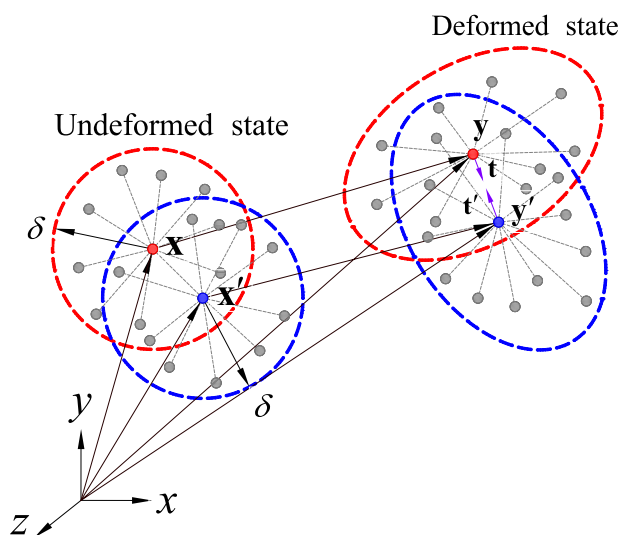


Fig. 1 Undeformed and deformed state of PD material points \mathbf{x} and \mathbf{x}'

when the force density vectors become equal in magnitude as well as being parallel to the relative position in the deformed state, the force function in the above Eq. (1) can be written as:

$$\mathbf{t}(\mathbf{u}' - \mathbf{u}, \mathbf{x}' - \mathbf{x}, t) = -\mathbf{t}'(\mathbf{u} - \mathbf{u}', \mathbf{x} - \mathbf{x}', t) = \frac{1}{2}\mathbf{f}(\mathbf{u}' - \mathbf{u}, \mathbf{x}' - \mathbf{x}, t) \tag{2}$$

where \mathbf{t} and \mathbf{f} represent the force density vector that material point \mathbf{x}' exerts on \mathbf{x} , as shown in Fig. 1.

Substituting Eq. (2) into Eq. (1), the motion equation of the bond-based PD (BBPD) can be obtained as:

$$\rho(\mathbf{x})\ddot{\mathbf{u}}(\mathbf{x}, t) = \int_H \mathbf{f}(\mathbf{u}' - \mathbf{u}, \mathbf{x}' - \mathbf{x}, t) dH + \mathbf{b}(\mathbf{x}, t) \tag{3}$$

where H is a neighborhood of the material point \mathbf{x} with a horizon radius δ , ρ represents the mass density, \mathbf{u} represents the displacement vector, and \mathbf{b} represents the body force density.

The PD equations of motion for laminated structures can be derived based on the principle of virtual work as:

$$\delta \int_{t_0}^{t_1} (T - U) dt = 0 \tag{4}$$

where T and U represent the kinetic and total potential energies, respectively.

The principle can be satisfied by solving for the Lagrange's equation as:

$$\frac{d}{dt} \left(\frac{\partial L}{\partial \dot{\mathbf{q}}_{(k)}} \right) - \frac{\partial L}{\partial \mathbf{q}_{(k)}} = 0 \tag{5}$$

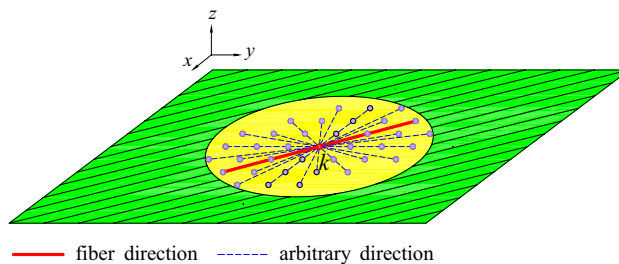


Fig. 2 PD horizon for a fiber-reinforced lamina and interaction of material points

where $\mathbf{q}_{(k)}$ represent independent displacement variables of the material point $\mathbf{x}_{(k)}$, and the Lagrangian function L is defined as:

$$L = T - U. \tag{6}$$

2.1 Peridynamic equations of motion

The total kinetic energy in the body due to twisting and bending can be expressed as:

$$T = \frac{1}{2} \rho \sum_{k=1}^{\infty} [\dot{u}_{(k)}^2 + \dot{v}_{(k)}^2 + \dot{w}_{(k)}^2] V_{(k)} \tag{7}$$

where u , v , and w represent the displacement components of material points in x -, y -, and z -directions, respectively. $V_{(k)}$ represents the volume of the current material point.

For a lamina subjected to out-of-plane bending or twisting, these in-plane variables can be expressed in terms of rotations as:

$$u_{(k)} = -z\phi_{x(k)}, \quad v_{(k)} = -z\phi_{y(k)}. \tag{8}$$

Integrating through the thickness direction of the lamina, the kinetic energy of the continuous system can be obtained as follows:

$$T = \frac{1}{2} h \rho \sum_{k=1}^{\infty} \left(\dot{w}_{(k)}^2 + \frac{h^2}{12} \dot{\phi}_{x(k)}^2 + \frac{h^2}{12} \dot{\phi}_{y(k)}^2 \right) A_{(k)} \tag{9}$$

where $A_{(k)}$ represents the area of the current material point and h denotes the thickness of the lamina.

Due to the unidirectional reinforcement properties, the directional dependency must be considered in the PD potential function for a composite lamina, as shown in Fig. 2. The total strain energy density can be decomposed as:

$$W_{(k)} = W_{(k)}^f + W_{(k)}^m \tag{10}$$

where $W_{(k)}^f$ and $W_{(k)}^m$ represent the contributions from fiber bonds and matrix bonds of the material point $\mathbf{x}_{(k)}$, respectively.

The total potential energy of a lamina can be expressed as:

$$U = \sum_{k=1}^{\infty} W_{(k)} - \sum_{k=1}^{\infty} \mathbf{b}_{(k)} \cdot \mathbf{u}_{(k)} = \sum_{k=1}^{\infty} W_{(k)}^f + \sum_{k=1}^J W_{(k)}^m - \sum_{k=1}^{\infty} \mathbf{b}_{(k)} \cdot \mathbf{u}_{(k)} \tag{11}$$

where J represents the number of fiber bonds in the horizon of the material point $\mathbf{x}_{(k)}$.

The strain energy density of material points can be obtained by summing micropotentials of all PD bonds in the horizon, as follows:

$$W_{(k)}^m = \frac{1}{2} \sum_{j=1}^{\infty} \frac{1}{2} \left[w_{(k)(j)}^m (y_{(1^k)} - y_{(k)}, y_{(2^k)} - y_{(k)}, \dots) + w_{(j)(k)}^m (y_{(1^j)} - y_{(j)}, y_{(2^j)} - y_{(j)}, \dots) \right] V_{(j)} \tag{12a}$$

$$W_{(k)}^f = \frac{1}{2} \sum_{j=1}^J \frac{1}{2} \left[w_{(k)(j)}^f (y_{(1^k)} - y_{(k)}, y_{(2^k)} - y_{(k)}, \dots) + w_{(j)(k)}^f (y_{(1^j)} - y_{(j)}, y_{(2^j)} - y_{(j)}, \dots) \right] V_{(j)} \tag{12b}$$

$$U = \sum_{k=1}^{\infty} \left\{ \frac{1}{2} \sum_{j=1}^J \frac{1}{2} \left[w_{(k)(j)}^f (\mathbf{y}_{(1^k)} - \mathbf{y}_{(k)}, \mathbf{y}_{(2^k)} - \mathbf{y}_{(k)}, \dots) + w_{(j)(k)}^f (\mathbf{y}_{(1^j)} - \mathbf{y}_{(j)}, \mathbf{y}_{(2^j)} - \mathbf{y}_{(j)}, \dots) \right] V_{(j)} + \frac{1}{2} \sum_{j=1}^{\infty} \frac{1}{2} \left[w_{(k)(j)}^m (\mathbf{y}_{(1^k)} - \mathbf{y}_{(k)}, \mathbf{y}_{(2^k)} - \mathbf{y}_{(k)}, \dots) + w_{(j)(k)}^m (\mathbf{y}_{(1^j)} - \mathbf{y}_{(j)}, \mathbf{y}_{(2^j)} - \mathbf{y}_{(j)}, \dots) \right] V_{(j)} - \frac{\bar{b}_{\alpha(k)}}{h} \phi_{\alpha(k)} \right\} V_{(k)} \quad (\alpha = x, y) \tag{13}$$

where $w_{(k)(j)}^m$ and $w_{(k)(j)}^f$ represent the micropotential function between the material points $\mathbf{x}_{(k)}$ and $\mathbf{x}_{(j)}$.

Substituting for the strain energy densities from Eq. (12) into Eq. (11), the total potential energy of a composite lamina in a deformed configuration can be rewritten as:

where $\bar{b}_{\alpha(k)}$ represents the resultant body moment at material point $\mathbf{x}_{(k)}$, and $\phi_{\alpha(k)}$ represents the degree of freedom of out-of-plane rotation.

To derive the equation of motion, the Lagrangian function in Eq. (6) can be expanded into the following formula, as follows:

$$\begin{aligned} L = & \dots + \rho_{(k)} \frac{h^3}{12} \dot{\phi}_{x(k)} \cdot \dot{\phi}_{x(k)} A_{(k)} + \rho_{(k)} \frac{h^3}{12} \dot{\phi}_{y(k)} \cdot \dot{\phi}_{y(k)} A_{(k)} + \dots \\ & - \frac{1}{2} \sum_{j=1}^J \left\{ w_{(k)(j)}^f (\mathbf{y}_{(1^k)} - \mathbf{y}_{(k)}, \mathbf{y}_{(2^k)} - \mathbf{y}_{(k)}, \dots) V_{(j)} V_{(k)} \right\} \dots \\ & - \frac{1}{2} \sum_{j=1}^J \left\{ w_{(j)(k)}^f (\mathbf{y}_{(1^j)} - \mathbf{y}_{(j)}, \mathbf{y}_{(2^j)} - \mathbf{y}_{(j)}, \dots) V_{(j)} V_{(k)} \right\} \dots \\ & - \frac{1}{2} \sum_{j=1}^{\infty} \left\{ w_{(k)(j)}^m (\mathbf{y}_{(1^k)} - \mathbf{y}_{(k)}, \mathbf{y}_{(2^k)} - \mathbf{y}_{(k)}, \dots) V_{(j)} V_{(k)} \right\} \dots \\ & - \frac{1}{2} \sum_{j=1}^{\infty} \left\{ w_{(j)(k)}^m (\mathbf{y}_{(1^j)} - \mathbf{y}_{(j)}, \mathbf{y}_{(2^j)} - \mathbf{y}_{(j)}, \dots) V_{(j)} V_{(k)} \right\} \dots + \frac{\bar{b}_{\alpha(k)}}{h} \phi_{\alpha(k)} V_{(k)}. \end{aligned} \tag{14}$$

For a plate or shell structure, the Euler–Lagrange equations can be written in terms of the degree of freedom of rotations as:

$$\frac{d}{dt} \frac{\partial L}{\partial \dot{\phi}_{\alpha(k)}} - \frac{\partial L}{\partial \phi_{\alpha(k)}} = 0 \quad (\alpha = x, y). \tag{15}$$

Therefore, the equations of motion describing the bending and twisting behavior of the lamina can be obtained when substituting Eq. (14) into Eq. (15) as:

$$\begin{aligned} \rho_{(k)} \frac{h^3}{12} \ddot{\phi}_{\alpha(k)} + \sum_{j=1}^{\infty} \frac{1}{2} \left(\sum_{i=1}^{\infty} \frac{\partial w_{(k)(i)}^m}{\partial (\mathbf{y}_{(j)} - \mathbf{y}_{(k)})} V_{(i)} \right) \frac{\partial (\mathbf{y}_{(j)} - \mathbf{y}_{(k)})}{\partial \mathbf{u}_{(k)}} \\ + \sum_{j=1}^{\infty} \frac{1}{2} \left(\sum_{i=1}^{\infty} \frac{\partial w_{(i)(k)}^m}{\partial (\mathbf{y}_{(k)} - \mathbf{y}_{(j)})} V_{(i)} \right) \frac{\partial (\mathbf{y}_{(k)} - \mathbf{y}_{(j)})}{\partial \mathbf{u}_{(k)}} \\ + \sum_{j=1}^J \frac{1}{2} \left(\sum_{i=1}^{\infty} \frac{\partial w_{(i)(k)}^f}{\partial (\mathbf{y}_{(k)} - \mathbf{y}_{(j)})} V_{(i)} \right) \frac{\partial (\mathbf{y}_{(k)} - \mathbf{y}_{(j)})}{\partial \mathbf{u}_{(k)}} \\ + \sum_{j=1}^J \frac{1}{2} \left(\sum_{i=1}^{\infty} \frac{\partial w_{(i)(k)}^f}{\partial (\mathbf{y}_{(k)} - \mathbf{y}_{(j)})} V_{(i)} \right) \frac{\partial (\mathbf{y}_{(k)} - \mathbf{y}_{(j)})}{\partial \mathbf{u}_{(k)}} - \frac{\bar{b}_{\alpha(k)}}{h} \phi_{\alpha(k)} = 0. \end{aligned} \tag{16}$$

In light of the definition of the strain energy densities in Eq. (13), the force density vectors can be derived in terms of micropotential functions, as follows:

$$f_{(k)(j)}^f = \frac{1}{\xi_{(j)(k)}} \frac{\partial w_{(k)(j)}^f}{\partial (\mathbf{y}_{(j)} - \mathbf{y}_{(k)})}, \quad f_{(j)(k)}^f = \frac{1}{\xi_{(k)(j)}} \frac{\partial w_{(j)(k)}^f}{\partial (\mathbf{y}_{(k)} - \mathbf{y}_{(j)})} \tag{17a, b}$$

and

$$f_{(k)(j)}^m = \frac{1}{\xi_{(j)(k)}} \frac{\partial w_{(k)(j)}^m}{\partial (\mathbf{y}_{(j)} - \mathbf{y}_{(k)})}, \quad f_{(j)(k)}^m = \frac{1}{\xi_{(k)(j)}} \frac{\partial w_{(j)(k)}^m}{\partial (\mathbf{y}_{(k)} - \mathbf{y}_{(j)})} \tag{18a, b}$$

where $f_{(k)(j)}^f$ and $f_{(j)(k)}^f$ represent force density vector of fiber bonds, $f_{(k)(j)}^m$ and $f_{(j)(k)}^m$ represent the force density vector of matrix bonds.

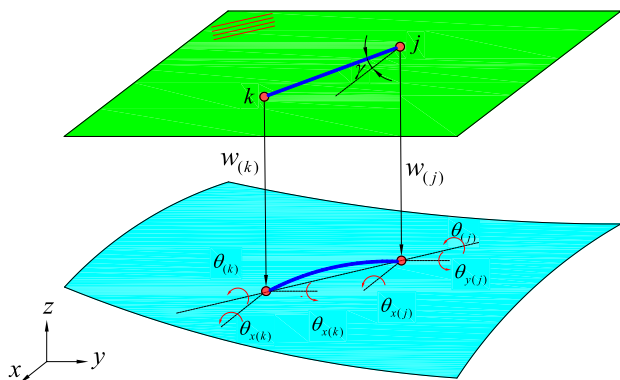


Fig. 3 Deformed and initial configuration of a lamina in PD

For a linear elastic material, the peridynamic micropotentials for a lamina due to bending can be written as:

$$w_{(k)(j)}^m = \frac{1}{2} c_m \kappa_{(k)(j)}^2 \xi_{(k)(j)} \tag{19a}$$

$$w_{(k)(j)}^f = \frac{1}{2} c_f \kappa_{(k)(j)}^2 \xi_{(k)(j)} \tag{19b}$$

where c_f and c_m represent micromodulus of fiber bonds and matrix bonds, respectively. $\kappa_{(k)(j)}$ represents the curvature with respect to the line of action between the material points $\mathbf{x}_{(j)}$ and $\mathbf{x}_{(k)}$, which can be defined as:

$$\kappa_{(k)(j)} = \frac{\phi_{(j)} - \phi_{(k)}}{\xi_{(j)(k)}} \tag{20}$$

where $\xi_{(j)(k)}$ represent distance between the material points $\mathbf{x}_{(j)}$ and $\mathbf{x}_{(k)}$. $\phi_{(j)}$ and $\phi_{(k)}$ represent the rotations with respect to the line of action between the material points $\mathbf{x}_{(j)}$ and $\mathbf{x}_{(k)}$.

The rotations with respect to the line of action between the material points $\mathbf{x}_{(j)}$ and $\mathbf{x}_{(k)}$ can be decomposed as

$$\phi_{(j)} = \phi_{x(j)} \cos \gamma + \phi_{y(j)} \sin \gamma \tag{21a}$$

$$\phi_{(k)} = \phi_{x(k)} \cos \gamma + \phi_{y(k)} \sin \gamma \tag{21b}$$

where γ represents the bond angle between $\mathbf{x}_{(j)}$ and $\mathbf{x}_{(k)}$ with respect to the x -axis, as shown in Fig. 3.

Substituting the above Eq. (21) into Eq. (20) yields the following expressions:

$$\kappa_{(k)(j)} = \left(\frac{\phi_{x(j)} - \phi_{x(k)}}{\xi_{(j)(k)}} \right) \cos \gamma + \left(\frac{\phi_{y(j)} - \phi_{y(k)}}{\xi_{(j)(k)}} \right) \sin \gamma \tag{22a}$$

or

$$\kappa_{(k)(j)} = \left(\frac{\phi_{x(j)} - \phi_{x(k)}}{x_{(j)} - x_{(k)}} \right) \cos^2 \gamma + \left(\frac{\phi_{y(j)} - \phi_{y(k)}}{y_{(j)} - y_{(k)}} \right) \sin^2 \gamma \tag{22b}$$

where

$$x_{(j)} - x_{(k)} = \xi_{(j)(k)} \cos \gamma \quad y_{(j)} - y_{(k)} = \xi_{(j)(k)} \sin \gamma. \tag{23a, b}$$

Substituting from Eq. (19) into Eqs. (17–18), the PD force density of the material point $\mathbf{x}_{(k)}$ can be obtained as:

$$f_{(k)(j)}^\alpha (\kappa_{(k)(j)}) = \frac{1}{\xi_{(k)(j)}} \frac{\partial w_{(k)(j)}^\alpha (\kappa_{(k)(j)})}{\partial (\kappa_{(k)(j)})} = c_\alpha \kappa_{(k)(j)} \quad (\alpha = x, y). \tag{24}$$

Hence, the Eq. (16) can be further written as:

$$\begin{aligned} &\rho \frac{h^3}{12} \ddot{\phi}_{\alpha(k)} + \sum_{j=1}^J \frac{1}{2} \xi_{jk} \left[f_{(k)(j)}^f \frac{\partial(\kappa_{(k)(j)})}{\partial(\phi_{\alpha(k)})} + f_{(j)(k)}^f \frac{\partial(\kappa_{(j)(k)})}{\partial(\phi_{\alpha(k)})} \right] V_{(j)} \\ &+ \sum_{j=1}^{\infty} \frac{1}{2} \xi_{jk} \left[f_{(k)(j)}^m \frac{\partial(\kappa_{(k)(j)})}{\partial(\phi_{\alpha(k)})} + f_{(j)(k)}^m \frac{\partial(\kappa_{(j)(k)})}{\partial(\phi_{\alpha(k)})} \right] V_{(j)} = 0. \end{aligned} \tag{25}$$

Invoking Eq. (22), and substituting from Eq. (24) into (25) yields the following equations of motion:

$$\begin{aligned} \rho \frac{h^3}{12} \ddot{\phi}_{x(k)} &= c_{\alpha} \sum_{j=1}^{\infty} \left[\left(\frac{\phi_{x(j)} - \phi_{x(k)}}{\xi_{(j)(k)}} \right) \cos \gamma + \left(\frac{\phi_{y(j)} - \phi_{y(k)}}{\xi_{(j)(k)}} \right) \sin \gamma \right] \\ &\cos \gamma V_{(j)} + \bar{b}_{x(k)} \end{aligned} \tag{26a}$$

$$\begin{aligned} \rho \frac{h^3}{12} \ddot{\phi}_{y(k)} &= c_{\alpha} \sum_{j=1}^{\infty} \left[\left(\frac{\phi_{x(j)} - \phi_{x(k)}}{\xi_{(j)(k)}} \right) \cos \gamma + \left(\frac{\phi_{y(j)} - \phi_{y(k)}}{\xi_{(j)(k)}} \right) \sin \gamma \right] \\ &\sin \gamma V_{(j)} + \bar{b}_{y(k)}. \end{aligned} \tag{26b}$$

The detailed derivation process on the PD material constants, c_f and c_m , is presented in Appendix 1. These material parameters describing the bending stiffness are presented as:

$$c_f = \frac{29h^2(q_{11} - q_{22})}{24\pi\delta^3} \quad c_m = \frac{2h^2q_{22}}{3\pi\delta^3} \tag{27a, b}$$

where q_{11} , q_{22} , q_{12} , and q_{66} represent the reduced stiffness coefficients of composite materials in the material coordinate system.

$$q_{11} = \frac{E_{11}}{1 - \nu_{12}\nu_{21}} \quad q_{22} = \frac{E_{22}}{1 - \nu_{12}\nu_{21}} \quad q_{12} = \frac{\nu_{12}E_{22}}{1 - \nu_{12}\nu_{21}} \quad q_{66} = G_{12} \tag{28}$$

where E_{11} , E_{22} , ν_{12} , ν_{21} and G_{12} are the elastic constants for orthotropic materials.

Since the PD material parameters, c_f and c_m , are derived for those material points whose horizon is complete. Therefore, these parameters need to be corrected for these material points located near a boundary or interface. The correction factors can be obtained by comparing the PD strain energy density to the counterpart in classical theory, which is presented in Appendix 2.

Although Eq. (26) can describe the out-of-plane mechanical behavior of composite materials, only the variation of rotations can be solved. The deflection of a lamina subjected to out-of-plane load cannot be simulated only by the above two equations. Therefore, the interpolation technique is essential in Sect. 2.2.

2.2 Interpolation technique

The transverse shear deformation is not considered in this PD model, and the normal is always perpendicular to the

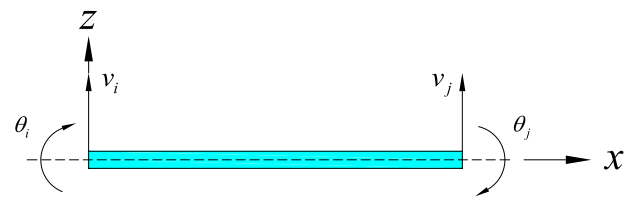


Fig. 4 Displacements and rotations of a PD bond

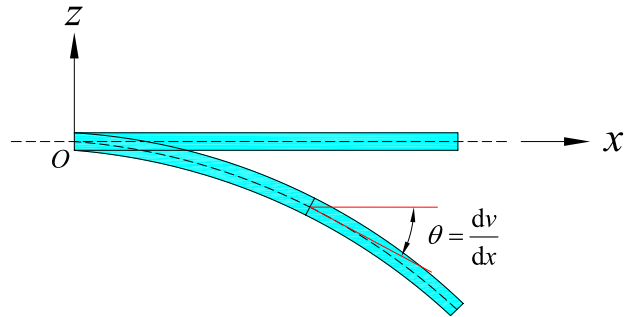


Fig. 5 Relationship between deflection and rotation

mid-plane of the laminate. Therefore, the differential equation of motion of PD bonds can be written as:

$$\rho A \frac{\partial^2 v}{\partial t^2} + \frac{\partial^2}{\partial x^2} \int_V \left(c_{\alpha} \frac{\partial^2 v}{\partial x^2} \right) dV = q \tag{29}$$

where v represents the transverse displacement of the PD bond, A and V represent the cross-sectional area and volume of the bond, c_{α} ($\alpha = f$ or m) represents the bending micro-modulus, and q represents the external load. t and x represent time and coordinates along the central axis of the bond, respectively.

Using the weighted residual method, the residual of Eq. (29) can be expressed as:

$$I = \int_0^{\xi} \left(\rho A \frac{\partial^2 v}{\partial t^2} + \frac{\partial^2}{\partial x^2} \int_V \left(c_{\alpha} \frac{\partial^2 v}{\partial x^2} \right) dV - q \right) w dx = 0 \tag{30}$$

where ξ and w represent the length and deflection of the bond, respectively.

Integrating the above Eq. (30) yields the following equations of motion as:

$$\begin{aligned} I &= \left[\int_0^{\xi} \rho A \frac{\partial^2 v}{\partial t^2} w dx + \int_0^{\xi} \int_V c_{\alpha} \frac{\partial^2 v}{\partial x^2} \frac{\partial^2 w}{\partial x^2} dV dx - \int_0^{\xi} \rho w dx \right] \\ &- \left[S w - M \frac{\partial w}{\partial x} \right]_0^{\xi} = 0 \end{aligned} \tag{31}$$

where

$$S = c_\alpha (\partial^3 v / \partial x^3) \quad M = c_\alpha (\partial^2 v / \partial x^2) \tag{32}$$

where S and M represent the shear and moment of the bond, respectively.

Due to the completeness and compatibility assumptions, the deflection of bonds can be characterized by a cubic polynomial function, as presented in Fig. 4, which can be expressed as:

$$v(x) = a_0 + a_1x + a_2x^2 + a_3x^3 \tag{33}$$

where $a_0, a_1, a_2,$ and a_3 represent the polynomial coefficients, and x represents the position of bonds in the local coordinate system ($0 \leq x \leq \xi$).

Since the PD model proposed in this paper is aimed at the Kirchhoff plate, as shown in Fig. 5, the rotation of bonds can be derived as:

$$\theta(x) = dv(x)/dx = a_1 + 2a_2x + 3a_3x^2. \tag{34}$$

For a PD bond consisting of two material points $\mathbf{x}_{(i)}$ and $\mathbf{x}_{(j)}$, its displacement vector can be expressed as:

$$\delta^e = [v_i \ \theta_i \ v_j \ \theta_j]^T. \tag{35}$$

Substituting the Eq. (35) into Eqs. (33) and (34), the expression can be written as:

$$\begin{cases} v(0) = a_0 = v_1 \\ \theta(0) = a_1 = \theta_1 \\ v(\xi) = a_0 + a_1\xi + a_2\xi^2 + a_3\xi^3 = v_2 \\ \theta(\xi) = a_1 + 2a_2\xi + 3a_3\xi^2 = \theta_2. \end{cases} \tag{36}$$

Equation (36) can be further written in matrix form as:

$$\delta^e = \begin{Bmatrix} v_i \\ \theta_i \\ v_j \\ \theta_j \end{Bmatrix} = \begin{bmatrix} 1 & 0 & 0 & 0 \\ 0 & 1 & 0 & 0 \\ 1 & \xi & \xi^2 & \xi^3 \\ 0 & 1 & 2\xi & 3\xi^2 \end{bmatrix} \begin{Bmatrix} a_0 \\ a_1 \\ a_2 \\ a_3 \end{Bmatrix} = \mathbf{A}\mathbf{C} \tag{37}$$

where

$$\mathbf{A} = \begin{bmatrix} 1 & 0 & 0 & 0 \\ 0 & 1 & 0 & 0 \\ 1 & \xi & \xi^2 & \xi^3 \\ 0 & 1 & 2\xi & 3\xi^2 \end{bmatrix}, \quad \mathbf{C} = \begin{Bmatrix} a_0 \\ a_1 \\ a_2 \\ a_3 \end{Bmatrix}. \tag{38a, b}$$

Solving Eq. (37) yields the parameter a_i ($i=0, 1, 2, 3$), and substituting these parameters a_i into Eq. (33) yields the following equation:

$$v(x) = N_1(x)v_i + N_2(x)\theta_i + N_3(x)v_j + N_4(x)\theta_j = [\mathbf{N}]\{\delta\}^e \tag{39}$$

where $[\mathbf{N}]$ is the shape function matrix of bonds, and its expression can be written as:

$$[\mathbf{N}] = [N_1 \ N_2 \ N_3 \ N_4] \tag{40}$$

where

$$N_1(x) = 1 - 3\chi^2 + 2\chi^3, \quad N_2(x) = (\chi - 2\chi^2 + \chi^3)\xi \tag{41a, b}$$

$$N_3(x) = 3\chi^2 - 2\chi^3, \quad N_4(x) = (-\chi^2 + \chi^3)\xi \tag{41c, d}$$

where $N_i(x)$ ($i=1, 2, 3, 4$) represents the Hermite function, χ represents the length of bonds, which can be expressed as:

$$\chi = x/\xi \quad (0 \leq \chi \leq 1). \tag{42}$$

Substituting the shape function matrix from Eq. (40) in Eq. (31) results in

$$\begin{aligned} & \int_0^\xi c_\alpha \frac{\partial^2 v}{\partial x^2} \frac{\partial^2 w}{\partial x^2} dx \\ &= \int_0^\xi c_\alpha \begin{Bmatrix} N_1'' \\ N_2'' \\ N_3'' \\ N_4'' \end{Bmatrix} \left[N_1'' \ N_2'' \ N_3'' \ N_4'' \right] dx \begin{Bmatrix} v_i \\ \theta_i \\ v_j \\ \theta_j \end{Bmatrix} \\ &= \int_0^\xi \mathbf{B}^T c_\alpha \mathbf{B} dx \delta^e = \mathbf{K}^e \delta^e \end{aligned} \tag{43}$$

where

$$[\mathbf{B}] = [N_1'' \ N_2'' \ N_3'' \ N_4'']^T. \tag{44}$$

Invoking Eqs. (41) and (44), and substituting for the integral equation from Eq. (43) in Eq. (31), the stiffness matrix of PD bonds can be obtained as:

$$\mathbf{K}^{PD} = \frac{c_\alpha V}{\xi^3} \begin{bmatrix} 12 & 6\xi & -12 & 6\xi \\ 6\xi & 4\xi^2 & -6\xi & 2\xi^2 \\ -12 & -6\xi & 12 & -6\xi \\ 6\xi & 2\xi^2 & -6\xi & 4\xi^2 \end{bmatrix}. \tag{45}$$

Substituting Eqs. (35) and (21) into the stiffness matrix in Eq. (45), the force density vector between material points $\mathbf{x}_{(k)}$ and $\mathbf{x}_{(j)}$ can be written in an explicit form as:

$$f_{(k)(j)} = c_\alpha \left[\begin{array}{l} 12(w_{(k)} - w_{(j)}) + 6\xi_{(k)(j)} (\theta_{x(k)} \sin \gamma - \theta_{y(k)} \cos \gamma) \\ + 6\xi_{(k)(j)} (\theta_{x(j)} \sin \gamma - \theta_{y(j)} \cos \gamma) \end{array} \right] V_{(j)} / \xi_{(k)(j)}^3 \tag{46a}$$

$$m_{(k)(j)} = c_\alpha \left[\begin{array}{l} 6\xi_{(k)(j)} (w_{(k)} - w_{(j)}) + 4\xi_{(k)(j)}^2 (\theta_{x(k)} \sin \gamma - \theta_{y(k)} \cos \gamma) \\ + 2\xi_{(k)(j)}^2 (\theta_{x(j)} \sin \gamma - \theta_{y(j)} \cos \gamma) \end{array} \right] V_{(j)} / \xi_{(k)(j)}^3. \tag{46b}$$

Hence, the equation of motion of composite materials can be written as:

$$\rho h \ddot{w}_{(k)} = \frac{c_\alpha}{\xi_{(k)(j)}^3} \sum_{j=1}^{\infty} \left[\begin{array}{l} 12w_{(j)} + 6\xi_{(j)(k)} (\phi_{x(k)} \sin \gamma - \phi_{y(k)} \cos \gamma) \\ - 12w_{(k)} + 6\xi_{(j)(k)} (\phi_{x(j)} \sin \gamma - \phi_{y(j)} \cos \gamma) \end{array} \right] V_{(j)} + b_{z(k)} \tag{47a}$$

$$\rho \frac{h^3}{12} \ddot{\phi}_{x(k)} = \frac{c_\alpha}{\xi_{(j)(k)}^3} \sum_{j=1}^{\infty} \left[\begin{array}{l} 6\xi_{(j)(k)} w_{(k)} + 4\xi_{(j)(k)}^2 (\phi_{x(k)} \sin \gamma - \phi_{y(k)} \cos \gamma) \\ - 6\xi_{(j)(k)} w_{(j)} + 2\xi_{(j)(k)}^2 (\phi_{x(j)} \sin \gamma - \phi_{y(j)} \cos \gamma) \end{array} \right] \sin \gamma V_{(j)} + m_{x(k)} \tag{47b}$$

$$\rho \frac{h^3}{12} \ddot{\phi}_{y(k)} = \frac{c_\alpha}{\xi_{(j)(k)}^3} \sum_{j=1}^{\infty} \left[\begin{array}{l} 6\xi_{(j)(k)} w_{(k)} + 4\xi_{(j)(k)}^2 (\phi_{x(k)} \sin \gamma - \phi_{y(k)} \cos \gamma) \\ - 6\xi_{(j)(k)} w_{(j)} + 2\xi_{(j)(k)}^2 (\phi_{x(j)} \sin \gamma - \phi_{y(j)} \cos \gamma) \end{array} \right] \cos \gamma V_{(j)} + m_{y(k)} \tag{47c}$$

or

$$\rho h \ddot{w}_{(k)} = \frac{c_\alpha}{\xi_{(j)(k)}^3} \sum_{j=1}^{\infty} \left[\begin{array}{l} 12w_{(j)} + 6\xi_{(j)(k)} (\phi_{x(k)} \sin \gamma - \phi_{y(k)} \cos \gamma) \\ - 12w_{(k)} + 6\xi_{(j)(k)} (\phi_{x(j)} \sin \gamma - \phi_{y(j)} \cos \gamma) \end{array} \right] V_{(j)} + b_{z(k)} \tag{48a}$$

$$\rho \frac{h^3}{12} \ddot{\phi}_{x(k)} = c_\alpha \sum_{j=1}^{\infty} \left[\left(\frac{\phi_{x(j)} - \phi_{x(k)}}{\xi_{(j)(k)}} \right) \cos \gamma - \left(\frac{\phi_{y(j)} - \phi_{y(k)}}{\xi_{(j)(k)}} \right) \sin \gamma \right] \cos \gamma V_{(j)} + m_{x(k)} \tag{48b}$$

$$\rho \frac{h^3}{12} \ddot{\phi}_{y(k)} = -c_\alpha \sum_{j=1}^{\infty} \left[\left(\frac{\phi_{x(j)} - \phi_{x(k)}}{\xi_{(j)(k)}} \right) \cos \gamma - \left(\frac{\phi_{y(j)} - \phi_{y(k)}}{\xi_{(j)(k)}} \right) \sin \gamma \right] \sin \gamma V_{(j)} + m_{y(k)}. \tag{48c}$$

The difference in sign between Eqs. (48b–48c) and (26a–26b) is that the rotations are represented in vector

form in Eq. (48). Compared with Eq. (26), the PD equations of motion in Eqs. (47) and (48) can better describe the out-of-plane mechanical behavior of unidirectional laminates, and the deflection and rotation can be simulated simultaneously.

2.3 Equations of motion for composite laminate

To describe the mechanical behavior of laminates, several assumptions are introduced: (1) There is no relative sliding and delamination between all adjacent plies, and the

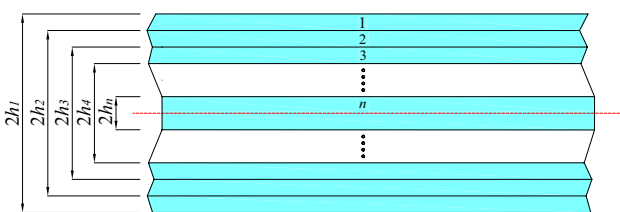


Fig. 6 Schematic of thickness coordinates of laminated structures

laminate is regarded as a whole structure, that is, the assumption of interlayer deformation compatibility needs to be satisfied; (2) Although the laminate is composed of multiple plies, its total thickness still satisfies the thin plate assumption, that is, the ratio of the thickness t to the span L is $(\frac{1}{50} \sim \frac{1}{100}) < \frac{t}{L} < (\frac{1}{8} \sim \frac{1}{10})$; (3) The whole laminate is of equal thickness.

The rotational equation of motion for the x -axis can be written as:

$$\rho \frac{h^3}{12} \ddot{\phi}_{(k)} = c \sum_{j=1}^{\infty} \left[\left(\frac{\phi_{x(j)} - \phi_{x(k)}}{\xi_{(j)(k)}} \right) \cos \gamma - \left(\frac{\phi_{y(j)} - \phi_{y(k)}}{\xi_{(j)(k)}} \right) \sin \gamma \right] V_{(j)} + b_{(k)}/A_{(k)} \tag{49}$$

where $b_{(k)}$ represent the moment.

For a laminate with n plies, as shown in Fig. 6, the equations of motion can be decomposed as:

$$\left\{ \begin{aligned} \rho \frac{(2h_1)^3 - (2h_2)^3}{12} \ddot{\phi}_{1(k)} &= c_1 \sum_{j=1}^{\infty} \left[\left(\frac{\phi_{1x(j)} - \phi_{1x(k)}}{\xi_{1(j)(k)}} \right) \cos \gamma - \left(\frac{\phi_{1y(j)} - \phi_{1y(k)}}{\xi_{1(j)(k)}} \right) \sin \gamma \right] V_{1(j)} + b_{1(k)}/A_{1(k)} \\ \rho \frac{(2h_2)^3 - (2h_3)^3}{12} \ddot{\phi}_{2(k)} &= c_2 \sum_{j=1}^{\infty} \left[\left(\frac{\phi_{2x(j)} - \phi_{2x(k)}}{\xi_{2(j)(k)}} \right) \cos \gamma - \left(\frac{\phi_{2y(j)} - \phi_{2y(k)}}{\xi_{2(j)(k)}} \right) \sin \gamma \right] V_{2(j)} + b_{2(k)}/A_{2(k)} \\ &\vdots \\ \rho \frac{(2h_n)^3}{12} \ddot{\phi}_{n(k)} &= c_n \sum_{j=1}^{\infty} \left[\left(\frac{\phi_{nx(j)} - \phi_{nx(k)}}{\xi_{n(j)(k)}} \right) \cos \gamma - \left(\frac{\phi_{ny(j)} - \phi_{ny(k)}}{\xi_{n(j)(k)}} \right) \sin \gamma \right] V_{n(j)} + b_{n(k)}/A_{n(k)}. \end{aligned} \right. \tag{50}$$

Due to the assumption of interlaminar deformation compatibility, the geometric relation in each ply can be obtained as:

$$\phi_{1x} = \phi_{2x} = \dots = \phi_{nx} \tag{51a}$$

$$\phi_{1y} = \phi_{2y} = \dots = \phi_{ny} \tag{51b}$$

$$\xi_{1(j)(k)} = \xi_{2(j)(k)} = \dots = \xi_{n(j)(k)} \tag{51c}$$

$$A_{1(k)} = A_{2(k)} = \dots = A_{n(k)}. \tag{51d}$$

Substituting these geometric relations from Eq. (51) into Eq. (50), and summing the system of Eq. (50) result in

$$\rho \bar{h} \ddot{w}_{(k)} = \frac{\bar{c}}{\xi_{(j)(k)}^3} \sum_{j=1}^{\infty} \left[\begin{aligned} &12w_{(j)} + 6\xi_{(j)(k)} (\phi_{x(k)} \sin \gamma - \phi_{y(k)} \cos \gamma) \\ &-12w_{(k)} + 6\xi_{(j)(k)} (\phi_{x(j)} \sin \gamma - \phi_{y(j)} \cos \gamma) \end{aligned} \right] \bar{V}_{(j)} + \bar{b}_{z(k)} \tag{55a}$$

$$\rho \frac{(2h_1)^3 - (2h_2)^3 + (2h_2)^3 - \dots + (2h_n)^3}{12} \ddot{\phi}_{(k)} = \sum_{j=1}^{\infty} \left\{ \begin{aligned} &(c_1 V_{1j} + c_2 V_{2j} + \dots + c_n V_{nj}) \\ &\times \left[\left(\frac{\phi_{x(j)} - \phi_{x(k)}}{\xi_{(j)(k)}} \right) \cos \gamma - \left(\frac{\phi_{y(j)} - \phi_{y(k)}}{\xi_{(j)(k)}} \right) \sin \gamma \right] \end{aligned} \right\} + \frac{b_{1(k)} + b_{2(k)} + \dots + b_{n(k)}}{A_{(k)}} \tag{52}$$

The above Eq. (52) can be further written as:

$$\rho \frac{\bar{h}^3}{12} \ddot{\phi}_{(k)} = \sum_{j=1}^{\infty} \bar{c}_{(j)(k)} \left[\left(\frac{\phi_{x(j)} - \phi_{x(k)}}{\xi_{(j)(k)}} \right) \cos \gamma - \left(\frac{\phi_{y(j)} - \phi_{y(k)}}{\xi_{(j)(k)}} \right) \sin \gamma \right] \bar{V}_{(j)} + \bar{b}_{(k)} \tag{53}$$

where \bar{c} represents the total bending micromodulus of the laminate, \bar{h} and \bar{V} represent the thickness and volume of the laminate, and \bar{b} represents the force per unit area. The

total thickness, volume, and bending micromodulus of the laminate can be obtained from all the plies as:

$$\bar{h} = \sum_{i=1}^n h_i \quad \bar{V} = \sum_{i=1}^n (A_i h_i) \tag{54a, b}$$

$$\bar{c} = \sum_{k=1}^{n/2} c_{\alpha} \left\{ \frac{[(n/2) + 1 - k] \times 2 \times h^2 - [(n/2) - k] \times 2 \times h^2}{12} \right\} \tag{54c}$$

where h_i and A_i represent the thickness and area of material points in the i -th ply, and h represents the thickness of each ply in the laminate.

Similarly, the equations of motion for Kirchhoff plates can also be obtained for other degrees of freedom. Hence, the equation of motion of the laminate can be expressed as:

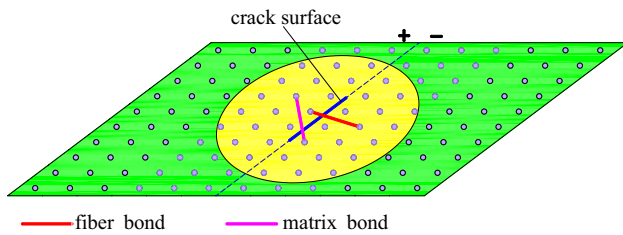


Fig. 7 Interaction between two material points whose line of action crosses the crack surface

$$\mu_\alpha(\mathbf{x}_{(j)} - \mathbf{x}_{(k)}, t) = \begin{cases} 1 & \text{if } \left| \kappa_{\alpha(k)(j)}(\mathbf{x}_{(j)} - \mathbf{x}_{(k)}, t) \right| < \kappa_{\alpha 0} \\ 0 & \text{otherwise} \end{cases} \tag{58}$$

where $\kappa_{\alpha 0}$ ($\alpha = f$ or m) represents the critical curvature of fiber bonds or matrix bonds.

The critical curvature of materials can be obtained according to the principle of energy equivalence. For a crack surface A in the lamina, the total strain energy stored in all broken bonds, including fiber bonds and matrix bonds, must

$$\rho \frac{\bar{h}^{-3}}{12} \ddot{\phi}_{x(k)} = \frac{\bar{c}}{\xi_{(j)(k)}^3} \sum_{j=1}^{\infty} \left[\begin{matrix} 6\xi_{(j)(k)}^2 w_{(k)} + 4\xi_{(j)(k)}^2 (\phi_{x(k)} \sin \gamma - \phi_{y(k)} \cos \gamma) \\ -6\xi_{(j)(k)} w_{(j)} + 2\xi_{(j)(k)}^2 (\phi_{x(j)} \sin \gamma - \phi_{y(j)} \cos \gamma) \end{matrix} \right] \sin \gamma \bar{V}_{(j)} + \bar{m}_{x(k)} \tag{55b}$$

$$\rho \frac{\bar{h}^{-3}}{12} \ddot{\phi}_{y(k)} = \frac{\bar{c}}{\xi_{(j)(k)}^3} \sum_{j=1}^{\infty} \left[\begin{matrix} 6\xi_{(j)(k)}^2 w_{(k)} + 4\xi_{(j)(k)}^2 (\phi_{x(k)} \sin \gamma - \phi_{y(k)} \cos \gamma) \\ -6\xi_{(j)(k)} w_{(j)} + 2\xi_{(j)(k)}^2 (\phi_{x(j)} \sin \gamma - \phi_{y(j)} \cos \gamma) \end{matrix} \right] \cos \gamma \bar{V}_{(j)} + \bar{m}_{y(k)} \tag{55c}$$

or

$$\rho \bar{h} \ddot{w}_{(k)} = \frac{\bar{c}}{\xi_{(j)(k)}^3} \sum_{j=1}^{\infty} \left[\begin{matrix} 12w_{(j)} + 6\xi_{(j)(k)} (\phi_{x(k)} \sin \gamma - \phi_{y(k)} \cos \gamma) \\ -12w_{(k)} + 6\xi_{(j)(k)} (\phi_{x(j)} \sin \gamma - \phi_{y(j)} \cos \gamma) \end{matrix} \right] \bar{V}_{(j)} + \bar{b}_{z(k)} \tag{56a}$$

$$\rho \frac{\bar{h}^{-3}}{12} \ddot{\phi}_{x(k)} = \bar{c} \sum_{j=1}^{\infty} \left[\left(\frac{\phi_{x(j)} - \phi_{x(k)}}{\xi_{(j)(k)}} \right) \cos \gamma - \left(\frac{\phi_{y(j)} - \phi_{y(k)}}{\xi_{(j)(k)}} \right) \sin \gamma \right] \cos \gamma \bar{V}_{(j)} + \bar{m}_{x(k)} \tag{56b}$$

$$\rho \frac{\bar{h}^{-3}}{12} \ddot{\phi}_{y(k)} = -\bar{c} \sum_{j=1}^{\infty} \left[\left(\frac{\phi_{x(j)} - \phi_{x(k)}}{\xi_{(j)(k)}} \right) \cos \gamma - \left(\frac{\phi_{y(j)} - \phi_{y(k)}}{\xi_{(j)(k)}} \right) \sin \gamma \right] \sin \gamma \bar{V}_{(j)} + \bar{m}_{y(k)}. \tag{56c}$$

3 Critical curvature and micromodulus reduction

In peridynamics, the damage to materials can be determined by counting the percentage of broken bonds by the total number of bonds. The force density vector will be permanently eliminated when the relative curvature between material points exceeds the critical value. The force and moment per unit area with damage can be expressed as follows:

$$\begin{cases} f_{(k)(j)}^\alpha = \mu_\alpha(\mathbf{x}_{(j)} - \mathbf{x}_{(k)}, t) \left[\begin{matrix} 12w_{(j)} + 6\xi_{(j)(k)} (\phi_{x(k)} \sin \gamma - \phi_{y(k)} \cos \gamma) \\ -12w_{(k)} + 6\xi_{(j)(k)} (\phi_{x(j)} \sin \gamma - \phi_{y(j)} \cos \gamma) \end{matrix} \right] & (\alpha = f \text{ or } m). \\ m_{(k)(j)}^\alpha = \mu_\alpha(\mathbf{x}_{(j)} - \mathbf{x}_{(k)}, t) c_\alpha \kappa_{(k)(j)} \end{cases} \tag{57}$$

be equal to the corresponding fracture energy in CCM, as shown in Fig. 7.

The strain energy stored in all broken bonds across the new crack surface A due to bending can be expressed as:

$$W_\alpha = \sum_{k=1}^{K^+} \sum_{j=1}^{j^-} \frac{1}{2} c_\alpha (\kappa_0)^2 \left(\left| \mathbf{x}_{(j^-)} - \mathbf{x}_{(k^+)} \right| \right) V_{(k^+)} V_{(j^-)}. \tag{59}$$

The state of PD bonds, intact or broken, can be defined as:

By equating Mode-I fracture energy release rate and the strain energy in Eq. (59), the critical curvature can be obtained as:

$$G_{IC} = \frac{\frac{1}{2}c_\alpha \kappa_0^2 \sum_{k=1}^{K^+} \sum_{j=1}^{J^-} \left(\left| \mathbf{x}_{(j^-)} - \mathbf{x}_{(k^+)} \right| \right) V_{(k^+)} V_{(j^-)}}{A} \quad (60)$$

where G_{IC} denotes the Mode-I fracture energy release rate of fiber or matrix material.

As introduced by Silling and Askari [3], the integral value in Eq. (60) can be obtained as:

$$\frac{\sum_{k=1}^{K^+} \sum_{j=1}^{J^-} \left(\left| \mathbf{x}_{(j^-)} - \mathbf{x}_{(k^+)} \right| \right) V_{(k^+)} V_{(j^-)}}{A} = \frac{h\delta^4}{2}. \quad (61)$$

Hence, the critical curvature of fiber bonds and matrix bonds can be obtained as:

$$\kappa_{0,\text{fiber}} = \sqrt{\frac{4G_1^{\text{fiber}}}{c_f h \delta^4}} \quad \kappa_{0,\text{matrix}} = \sqrt{\frac{4G_1^{\text{matrix}}}{c_m h \delta^4}} \quad (62a, b)$$

where $\kappa_{0,\text{fiber}}$ and $\kappa_{0,\text{matrix}}$ represent the critical curvature of fiber bonds and matrix bonds, respectively. G_1^{fiber} and G_1^{matrix} represent the Mode-I fracture energy release rate of fiber and matrix material, respectively.

For laminated structures, damage in each ply needs to be examined at each time step, and the corresponding total micromodulus of laminates needs to be updated all the time as:

$$\bar{c}^{\text{update}} = \sum_{k=1}^{n/2} c_n^{\text{update}} \left\{ \frac{[(n/2) + 1 - k] \times 2 \times h]^2 - [(n/2) - k] \times 2 \times h]^2}{12} \right\} \quad (63)$$

where \bar{c}^{update} represents the updated micromodulus of laminates, c_n^{update} represents the updated micromodulus between material points in the n -th ply of laminates, which can be expressed as:

$$c_n^{\text{update}} = \begin{cases} c_n & \text{if } \left| \kappa_{n(k)(j)}(\mathbf{x}_{(j)} - \mathbf{x}_{(k)}, t) \right| < \kappa_{n0} \\ 0 & \text{otherwise} \end{cases} \quad (64)$$

where $\kappa_{n(k)(j)}(\mathbf{x}_{(j)} - \mathbf{x}_{(k)}, t)$ represents the curvature in the n -th ply of laminates between material points $\mathbf{x}_{(j)}$ and $\mathbf{x}_{(k)}$ at time t .

4 Numerical solution method

The adaptive dynamic relaxation method (ADR) [53, 54] is used to solve the equations for static and quasi-static problems. In addition to the virtual mass matrix \mathbf{M} , virtual damping d_c^n also needs to be introduced in Eqs. (55)–(56) for composite laminates as

$$\mathbf{M}\ddot{\mathbf{U}}^n(\mathbf{X}, t) + d_c^n \mathbf{M}\dot{\mathbf{U}}^n(\mathbf{X}, t) = \mathbf{F}^n(\mathbf{U}, \mathbf{U}', \mathbf{X}, \mathbf{X}') \quad (65)$$

where \mathbf{X} and \mathbf{U} represent the initial position and displacement, respectively. \mathbf{X}' and \mathbf{U}' represent the position and displacement of material points in a deformed configuration, respectively. \mathbf{F} represents the load, including the internal force and area force.

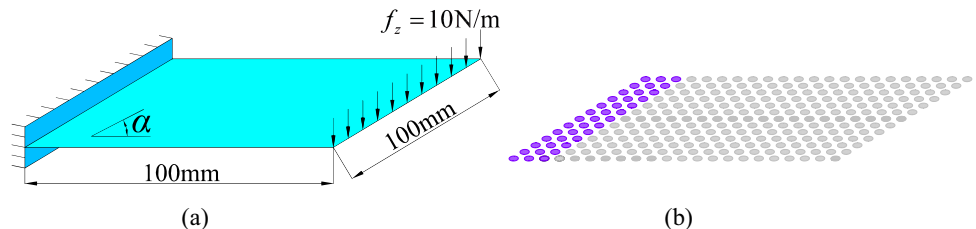
$$\mathbf{F}_k = \sum_{j=1}^{N_k} G_{(k)(j)} \mu(\mathbf{x}_{(j)} - \mathbf{x}_{(k)}, t) \mathbf{f}(\mathbf{u}_j - \mathbf{u}_k, \mathbf{x}_j - \mathbf{x}_k) C_{V_j} V_j + \mathbf{b}_k \quad (66)$$

where $G_{(k)(j)}$ represents the correction factor between $\mathbf{x}_{(k)}$ and $\mathbf{x}_{(j)}$, which is provided in Appendix 2. C_{V_j} represents a correction parameter, which is defined as:

$$C_{V_j} = \begin{cases} 0 & \|\boldsymbol{\eta} + \boldsymbol{\xi}\| \geq \delta \\ 1 & \|\boldsymbol{\eta} + \boldsymbol{\xi}\| \leq (\delta - r) \\ \frac{\delta + r - \|\boldsymbol{\eta} + \boldsymbol{\xi}\|}{2r} & (\delta - r) \leq \|\boldsymbol{\eta} + \boldsymbol{\xi}\| \leq \delta \end{cases} \quad (67)$$

where $r = \Delta x/2$.

Fig. 8 Lamina subjected to static bending **a** geometry, **b** model discretization



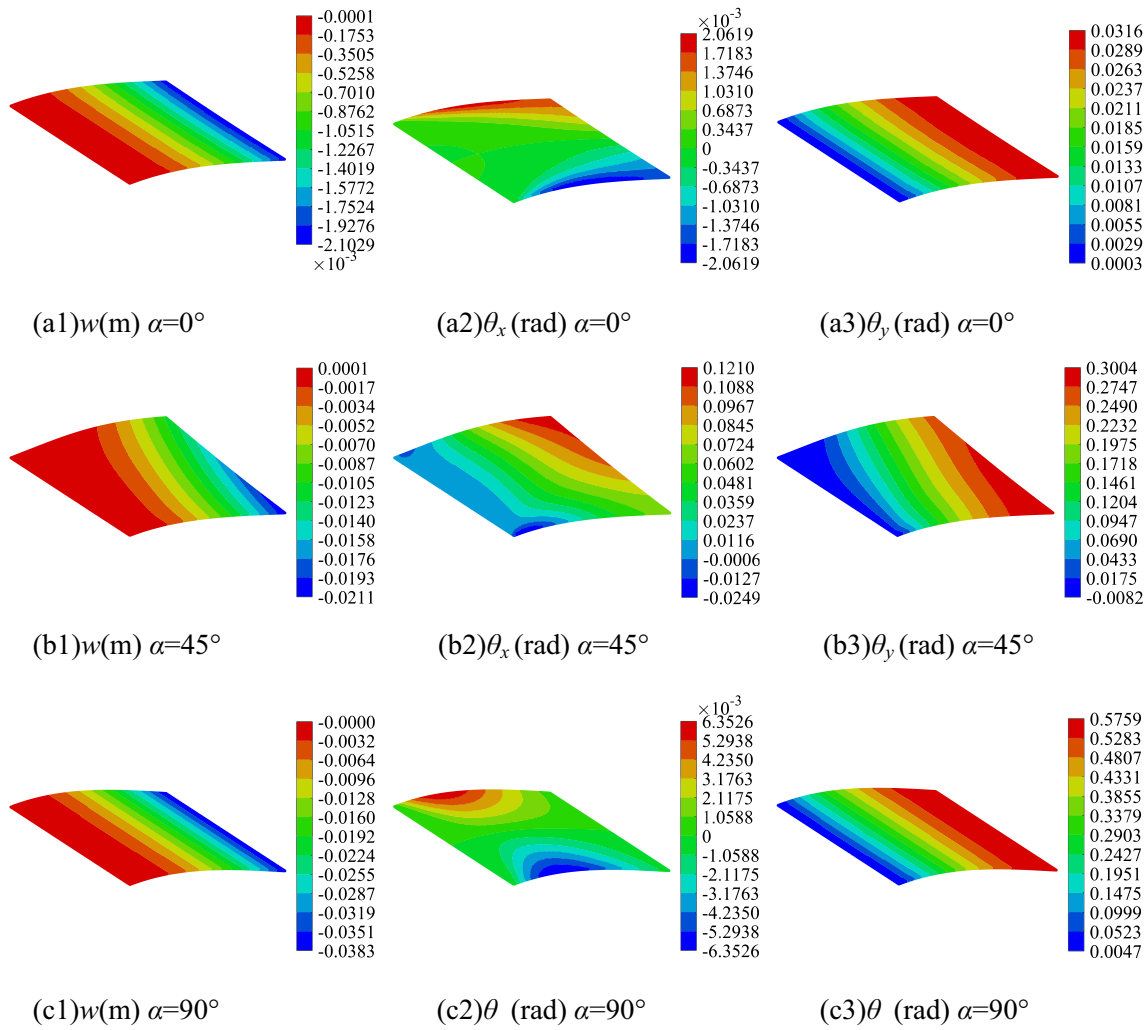


Fig. 9 Predicted displacement and rotation variations of unidirectional laminates with different fiber orientations from PD analysis

Both the virtual density matrix and the stiffness matrix are diagonal, and the diagonal terms can be expressed as:

$$\mathbf{M}_{(k)} = \begin{bmatrix} M_{w(k)} & 0 & 0 \\ 0 & M_{\theta_{x(k)}} & 0 \\ 0 & 0 & M_{\theta_{y(k)}} \end{bmatrix} \quad (68)$$

where $M_{w(k)}, M_{\theta_{x(k)}, M_{\theta_{y(k)}}$ represent the components of the mass stable vector corresponding to translational and rotational DOFs, which can be calculated as:

$$M_{w(k)} \geq \frac{1}{4} \Delta t^2 \frac{C_s \pi h \delta^2}{\Delta x} \quad M_{\theta_{x(k)}} = M_{\theta_{y(k)}} = \frac{1}{4} \Delta t^2 \frac{c_\alpha \pi h \delta^2}{\Delta x} \quad (69a, b)$$

where Δx represents grid spacing, $\Delta t = 1$ represents the time step for a quasi-static solution, c_α represents PD material parameters for bending deformation given in Eq. (27). C_s

represents the shear constant in the transverse direction, which is defined as:

$$C_s = \frac{3k_s}{\pi \delta^3} \frac{E_{22}}{(1 + \nu_{12})} \quad (70)$$

where $k_s = 5/6$ represents the shear correction factor.

The damping factor can be determined by the lowest frequency of the system as:

$$d_c^n = 2 \sqrt{\frac{(\mathbf{U}^n)^T \mathbf{K}^n \mathbf{U}^n}{(\mathbf{U}^n)^T \mathbf{M}^n \mathbf{U}^n}} \quad (71)$$

By utilizing central-difference explicit integration, the velocities of the n -th step can be obtained as:

$$\dot{\mathbf{U}}^n = \mathbf{U}^{n-\frac{1}{2}} + \frac{1}{2} \ddot{\mathbf{U}}^n \Delta t \quad (72)$$

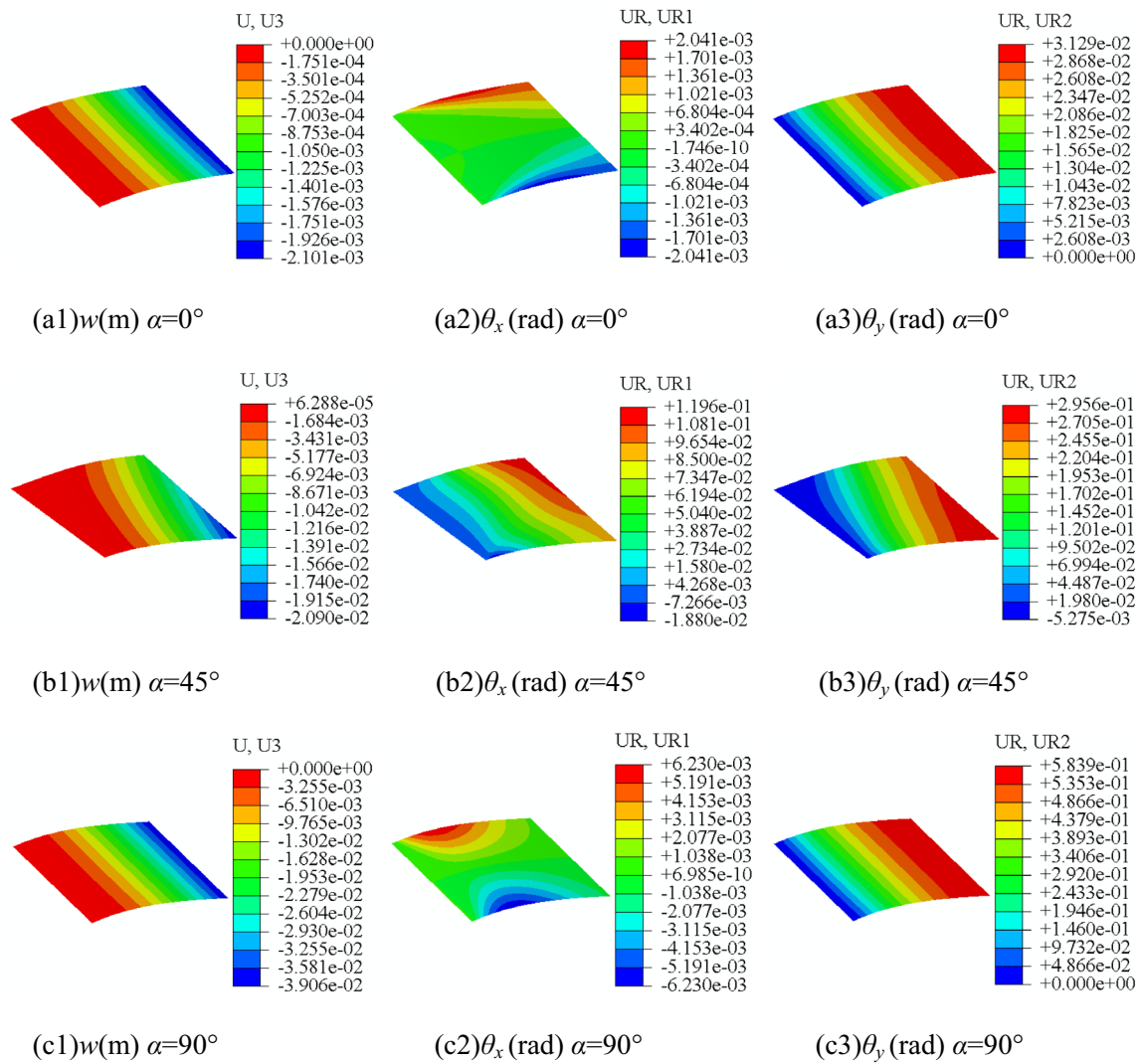


Fig. 10 Predicted displacement and rotation variations of unidirectional laminates with different fiber orientations from FE analysis

Then the displacement for the next time step can be obtained as:

$$\mathbf{U}^{n+1} = \mathbf{U}^n + \dot{\mathbf{U}}^{n+\frac{1}{2}} \Delta t \tag{73}$$

$$\dot{\mathbf{U}}^{n+\frac{1}{2}} = \frac{(2 - d_c^n \Delta t) \dot{\mathbf{U}}^{n-\frac{1}{2}} + 2\mathbf{M}^{-1}\mathbf{F}^n \Delta t}{2 + d_c^n \Delta t} \tag{74}$$

Supposing $\mathbf{U}^0 \neq 0, \dot{\mathbf{U}}^{-1/2} = 0$, the initial velocity is given by

$$\dot{\mathbf{U}}^{\frac{1}{2}} = \frac{\mathbf{M}^{-1}\mathbf{F}^0 \Delta t}{2} \tag{75}$$

5 Validation and demonstration

Numerical results aim at first the verification of the PD model by capturing the expected deformation response of composite laminates under general load conditions in Sects. 5.1 and 5.2. Subsequently, the proposed PD model is used to predict the damage pattern of laminates subjected to four-point bending in Sect. 5.3. Finally, in Sect. 5.4, the challenging benchmark on the DCB Test was also simulated.

5.1 Lamina with different fiber orientations subjected to constant static bending

Based on this PD model, three unidirectional laminates with $\alpha=0^\circ, 45^\circ, \text{ and } 90^\circ$ were analyzed in this section.

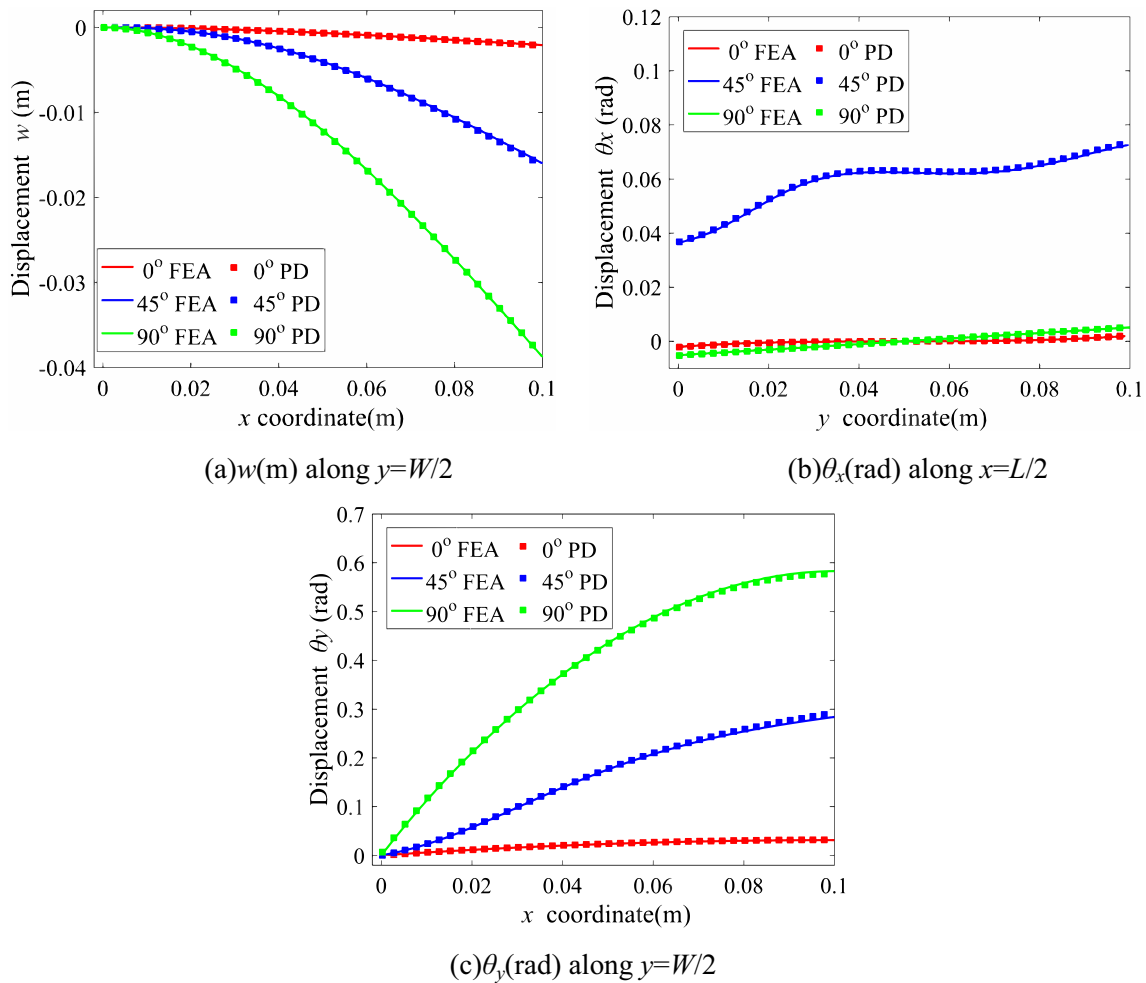


Fig. 11 Comparison of predicted variations w (m), θ_x (rad), and θ_y (rad)

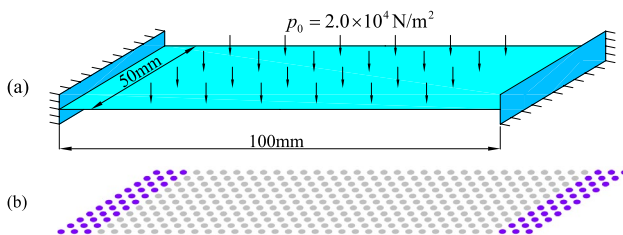


Fig. 12 Laminate subjected to static pressure **a** geometry, **b** model discretization

As shown in Fig. 8a, the square lamina has dimensions of $L \times W = 100 \text{ mm} \times 100 \text{ mm}$ and thickness of $h = 0.5 \text{ mm}$. The lamina is fixed on the left edge, and it is subjected to uniformly distributed load $f_z = 10 \text{ N/m}$ perpendicular to the surface on the right edge of the lamina. In the PD model,

the constant distributed load needs to be converted to area forces for the material points located at $x = L$.

Material properties for the lamina are: The mass density $\rho = 1580 \text{ kg/m}^3$, Young’s modulus in fiber direction $E_{11} = 1.55 \times 10^{11} \text{ Pa}$, Young’s modulus in transverse direction $E_{22} = 8.3 \times 10^9 \text{ Pa}$, in-plane Poisson’s ratio $\nu_{12} = 0.33$, in-plane shear modulus $G_{12} = 2.77 \times 10^9 \text{ Pa}$. To apply boundary conditions on the left edge of the lamina, three fictitious layers of material points are generated in the discrete model as shown in Fig. 8b, and all displacement components of these material points located at $x \leq 0$ are set equal to zero. The lamina is discretized with a uniform grid of 200×200 leading to 120,000 degrees of freedom. For verification purposes, the predictions from the proposed PD model are compared against FEA solutions conducted using ABAQUS commercial software. In the FEA model, the same mesh size is used. In ADR, the time step is set to $dt = 1$, and the problem is simulated in 300,000, 2,000,000, and 1,000,000

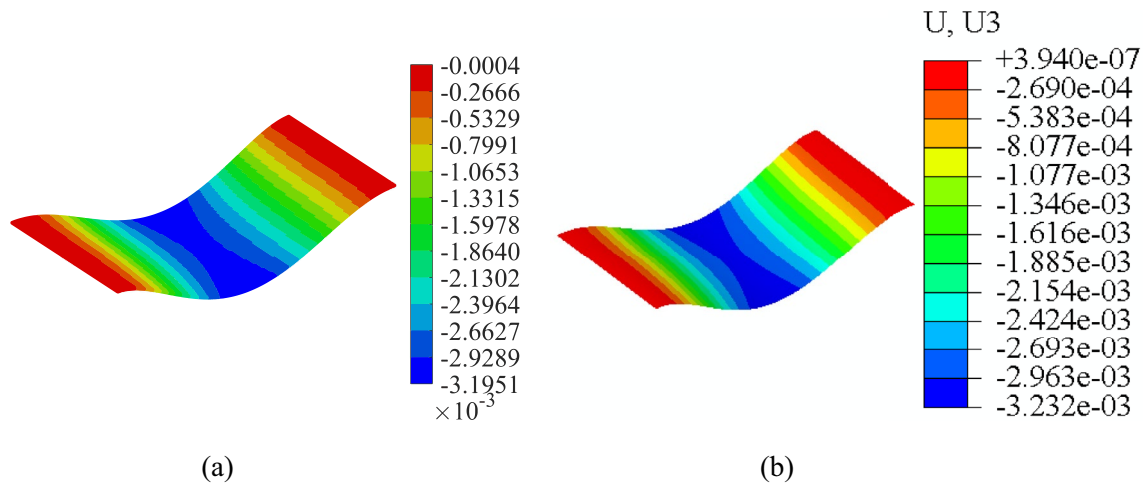


Fig. 13 Variation of displacement w (m) in deformed configuration **a** PD, **b** FEA results

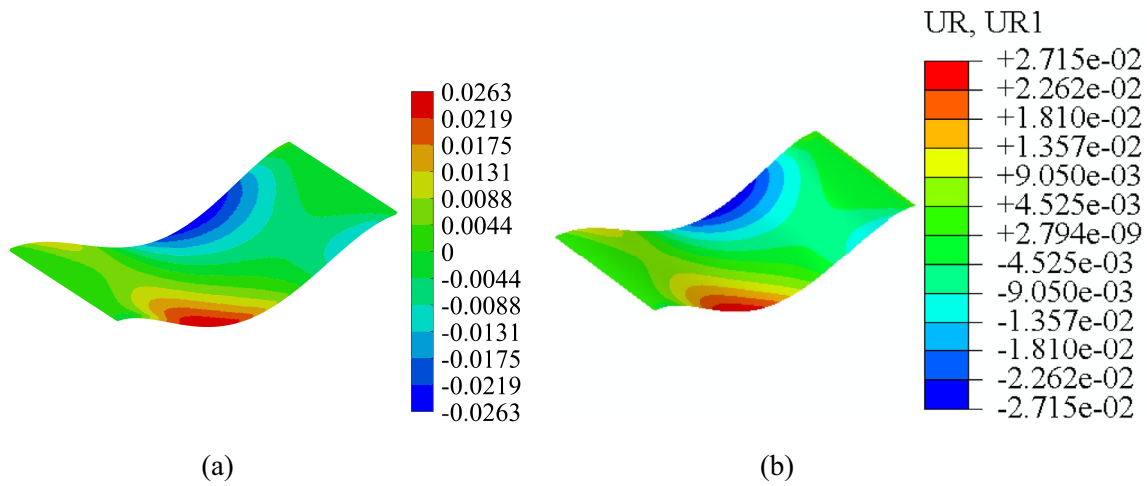


Fig. 14 Variation of rotation θ_x (rad) in deformed configuration **a** PD, **b** FEA results

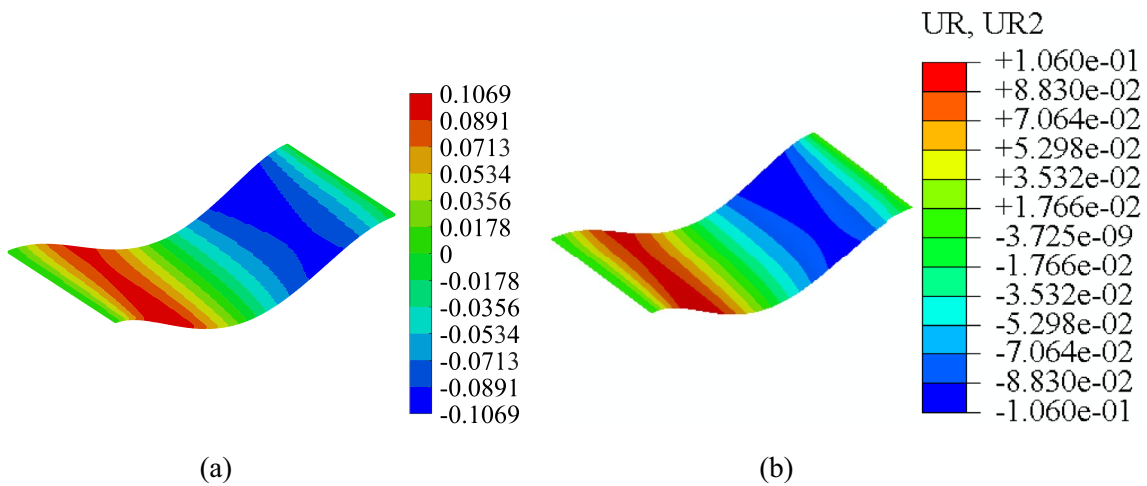


Fig. 15 Variation of rotation θ_y (rad) in deformed configuration **a** PD, **b** FEA results

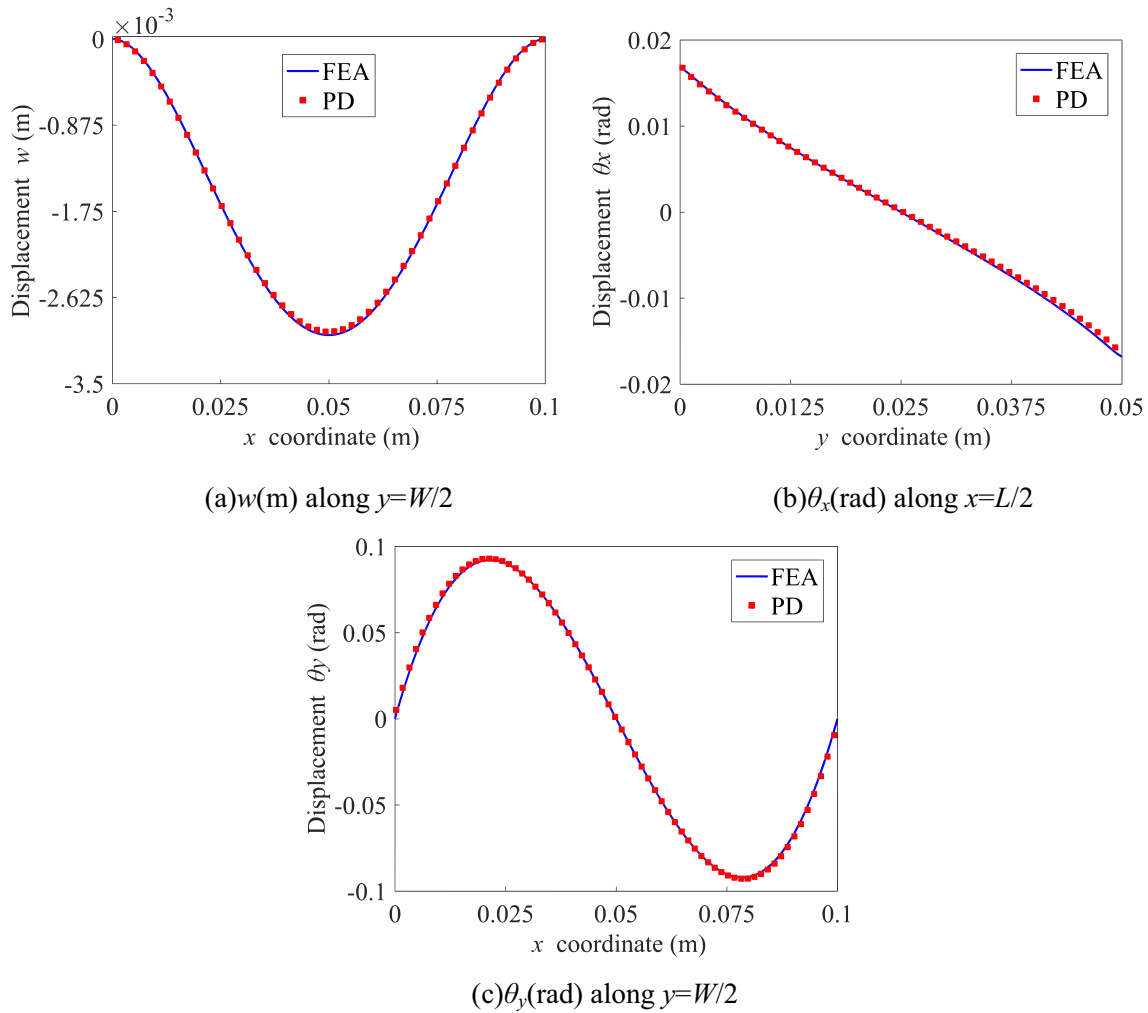


Fig. 16 Comparison of predicted variations w (m), θ_x (rad), and θ_y (rad)

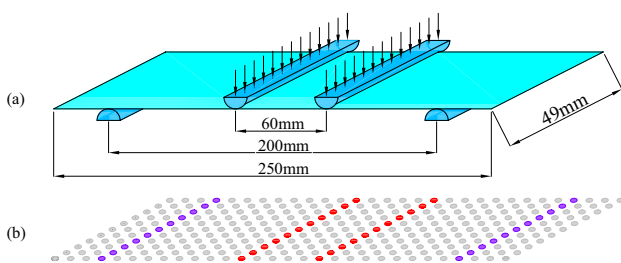


Fig. 17 Laminate subjected to four-point bending **a** geometry, **b** model discretization

load steps corresponding to the lamina with $\alpha=0^\circ$, 45° , and 90° , respectively. Figures 9 and 10 show the variations of 3 DOFs of the three laminates in the deformed configuration.

As can be seen from Figs. 9 and 10, the variations of displacement w and rotations θ_x and θ_y captured by the developed PD model agree very well with FEA results for the three laminates. Therefore, the numerical accuracy of the

PD model can be verified. To have a better comparison, the PD and FEA solution results along $y = W/2$ and $x = L/2$ are compared as shown in Fig. 11.

It can be observed from Fig. 11 that the relative errors between PD and FEA results for all DOFs are less than 1.97% for these three laminates, indicating an excellent agreement. A conclusion can be drawn from this example that the developed PD model has a strong capacity to capture the out-of-plane mechanical behavior of composite lamina with reliable numerical accuracy.

5.2 Laminate subjected to constant static bending

To further verify the proposed PD model for laminates, a rectangular composite lamina with $L \times W = 100 \text{ mm} \times 50 \text{ mm}$ is investigated as shown in Fig. 12a. The lamina has a layout of $[45/0/90]_{6s}$ with ply thickness $h = 0.0187 \text{ mm}$. The material properties of the lamina are identical to the lamina in Sect. 5.1. The lamina is fully clamped on the left

Fig. 18 Damage pattern on the laminate subjected to four-point bending with z -direction displacement of **a** $w=15$ mm, **b** $w=18.75$ mm, **c** $w=22.5$ mm, **d** $w=26.25$ mm, and **e** $w=30$ mm

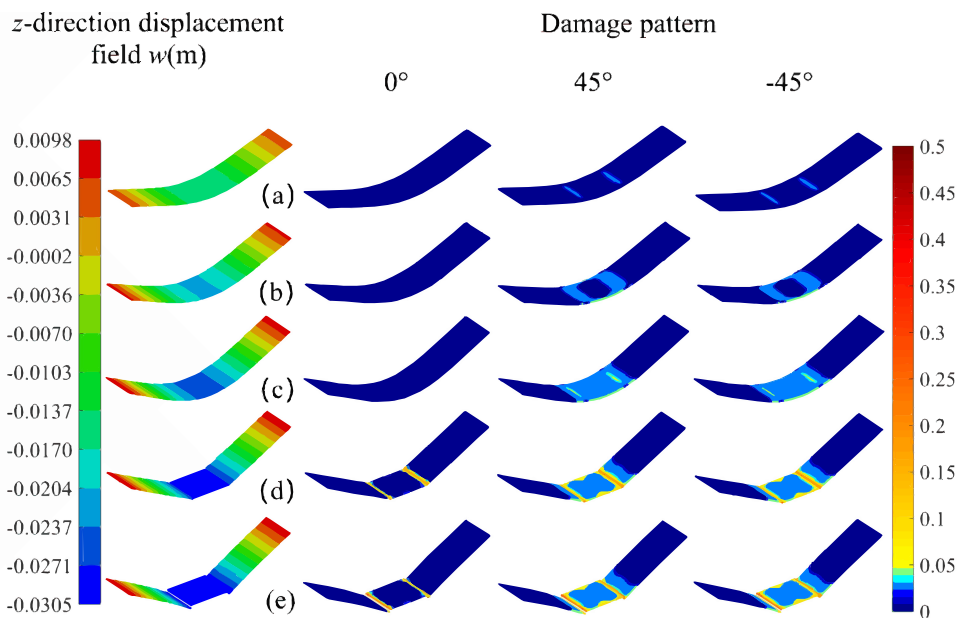
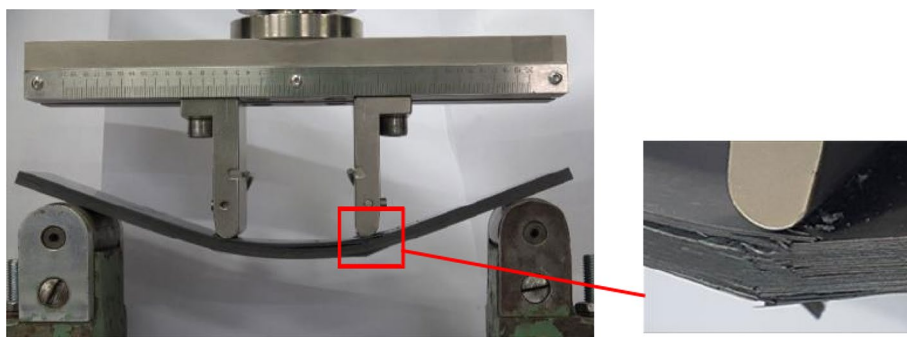


Fig. 19 Experimental results: damage pattern of the laminate [55]



and right edges, and it is subjected to transverse pressure of $p_0=2.0 \times 10^4$ N/m² normal to the top surface.

In peridynamic model, a uniform in-plane grid of 200×100 is achieved in the discrete model, and only single-layer material points exist in the thickness direction leading to a total degree of freedom of 60,000 for the laminate. To apply the clamped boundary condition, three fictitious layers of material points are added to both edges of the laminate as shown in Fig. 12b, and all DOFs of these fictitious points are set equal to zero. To verify the accuracy of the developed PD model for the laminate, FE analysis is carried out to simulate the example, and the mesh size is $\Delta x=5.0 \times 10^{-4}$ m. The explicit time integration is used for the static problem by using the adaptive dynamic relaxation (ADR) method, and 10 million load steps are set in this PD simulation. Figures 13, 14 and 15 present the comparison of PD and ABAQUS predictions for displacement and rotation of 3 DOFs with $\delta=3.015\Delta x$ in the deformed configuration.

Figures 13, 14 and 15 show the deformation contours of the laminate obtained from FE and PD analyses. It is evident that

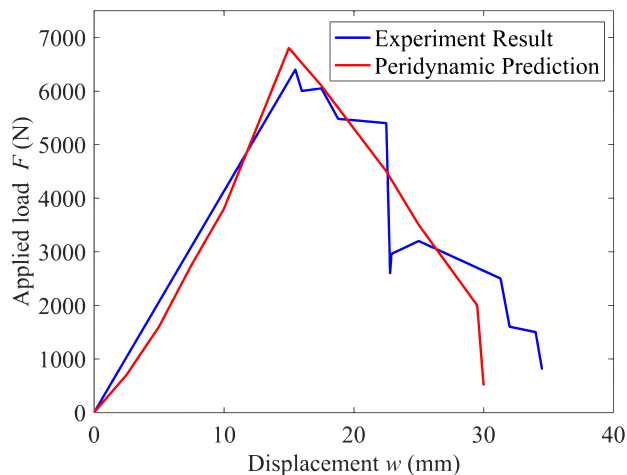


Fig. 20 Load–displacement relations for the laminate

FEA and PD results have an excellent agreement, which demonstrates the accuracy of this proposed PD. Similar to previous examples, the displacement and rotation at $(y=W/2, x=L/2)$ obtained from PD and FEA are compared as shown in Fig. 16. As can be seen, the PD predictions for all degrees of freedom of the laminate have good agreement with the FEA solution, and the relative error for all displacement components are less than 3.13%. Two possible reasons for this difference are: (1) Higher order elements are used in ABAQUS analysis; (2) Transverse shear deformation affects FE results. Nevertheless, it can still be concluded that the developed PD model can well characterize the mechanical behavior of laminated structures and high numerical accuracy can be expected.

In addition to the advantage in describing the out-of-plane mechanical behavior of anisotropic materials, it has been demonstrated through this example that the multi-layer laminated structure can be simulated with single-layer material points in the proposed PD model and the numerical accuracy can be well ensured. Since each ply does not need to be uniformly discretized for the laminate, the number of material points will be greatly reduced in the discrete model, and the computational efficiency can be significantly improved in comparison with the traditional multi-layer PD model.

5.3 Damage prediction in a laminate subjected to four-point bending

After verifying the accuracy of the developed PD model for laminated structures, the damage process in a laminate subjected to four-point bending is investigated. The experiment was conducted by Qian [55]. The laminate has dimensions of $L \times B \times H = 250 \times 49 \times 5.8 \text{ mm}^3$, and the detailed geometric layout is illustrated in Fig. 17a. The laminate has a layup of $[0/45/0/-45]_{4s}$ with ply thickness $h = 0.18 \text{ mm}$.

The material properties of the laminate are specified as: $E_{11} = 1.25 \times 10^{11} \text{ Pa}$, $E_{22} = 1.08 \times 10^{10} \text{ Pa}$, $G_{12} = 3.6 \times 10^9 \text{ Pa}$,

and $\nu_{12} = 0.33$. The strength properties are: longitudinal tensile strength $X_t = 2213 \text{ MPa}$, longitudinal compressive strength $X_c = 706 \text{ MPa}$, transverse tensile strength $Y_t = 24.5 \text{ MPa}$, and transverse compressive strength $Y_c = 125 \text{ MPa}$. The laminate was simply supported at $x = \pm 0.4L$ (these purple points in Fig. 17b), and the boundary condition is applied by setting displacement component w of these material points located at $x = \pm 0.4L$ to zero at each time step. In loading regions, the laminate is subjected to a slow rate of stretch of $1.0 \times 10^{-8} \text{ m/s}$ in the z -direction for these material points located at $x = \pm 0.12L$ (these red points in Fig. 17b), representing quasi-static loading. The horizon size is $\delta = 3.015\Delta x$, and grid spacing is specified as $\Delta x = 1.0 \text{ mm}$. The in-plane discretization is achieved with 250×50 material points, which results in 37,500 degrees of freedom in the PD model. The adaptive dynamic relaxation methodology is used in the PD solution for the quasi-static problem. Since single-layer material point is used to describe the mechanical behavior of multi-layer laminate, therefore, for material points with the same in-plane coordinates, the deformation curvature is the same in different plies at each time step. Moreover, the damage pattern is the same in each ply with the same fiber orientations. As the load increases, the displacement contours of the laminate and damage patterns in 0° and $\pm 45^\circ$ plies at different time steps are presented in Fig. 18.

Figure 18 shows the damage evolution in each ply on the laminate subjected to four-point bending. As shown in Fig. 18a, when the applied displacement is $w = 15 \text{ mm}$, damage in $\pm 45^\circ$ plies initiates at the loading region due to stress concentration, at $(x = \pm 0.12L)$. As the applied displacements are increased, the damage propagates toward both sides of the loading region and merges in the middle of the laminate, as shown in Fig. 18b, c. When the applied displacement is $w = 26.25 \text{ mm}$, damage in 0° ply occurs at the loading region as shown in Fig. 18d. When the applied displacement is $w = 30 \text{ mm}$, the crack opens largely at the loading region, and the laminate is almost split into three parts as shown in Fig. 18e.

Since the number of $\pm 45^\circ$ plies in the laminate is equal, the reinforcement degree of the laminate is the same in the x - and y -directions. Therefore, damage in $\pm 45^\circ$ plies is mainly matrix cracking, and the corresponding displacement contours are still continuous even when matrix damage occurs. Moreover, the damage evolves symmetrically with the y -axis at all times. Because the strength of resin materials is weaker than that of the carbon fiber, damage in $\pm 45^\circ$ plies occurs earlier than that in the 0° ply, and the damaged area is larger. Since the damage mechanism is mainly fiber breakage in the 0° ply, the overall failure of the laminate occurs accompanied by the 0° ply. As shown in Fig. 18d, the displacement contour presents an obvious discontinuity.

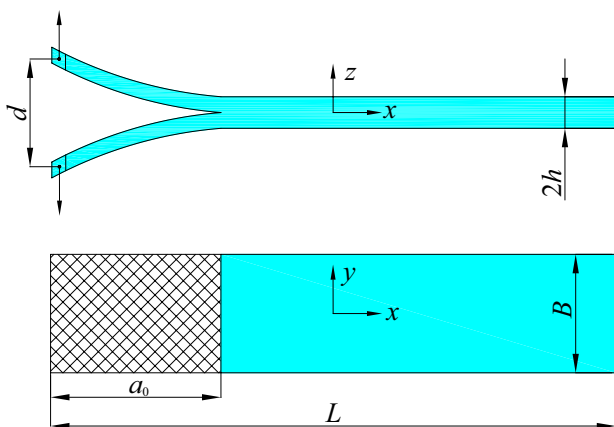


Fig. 21 Geometry and boundary conditions of DCB test

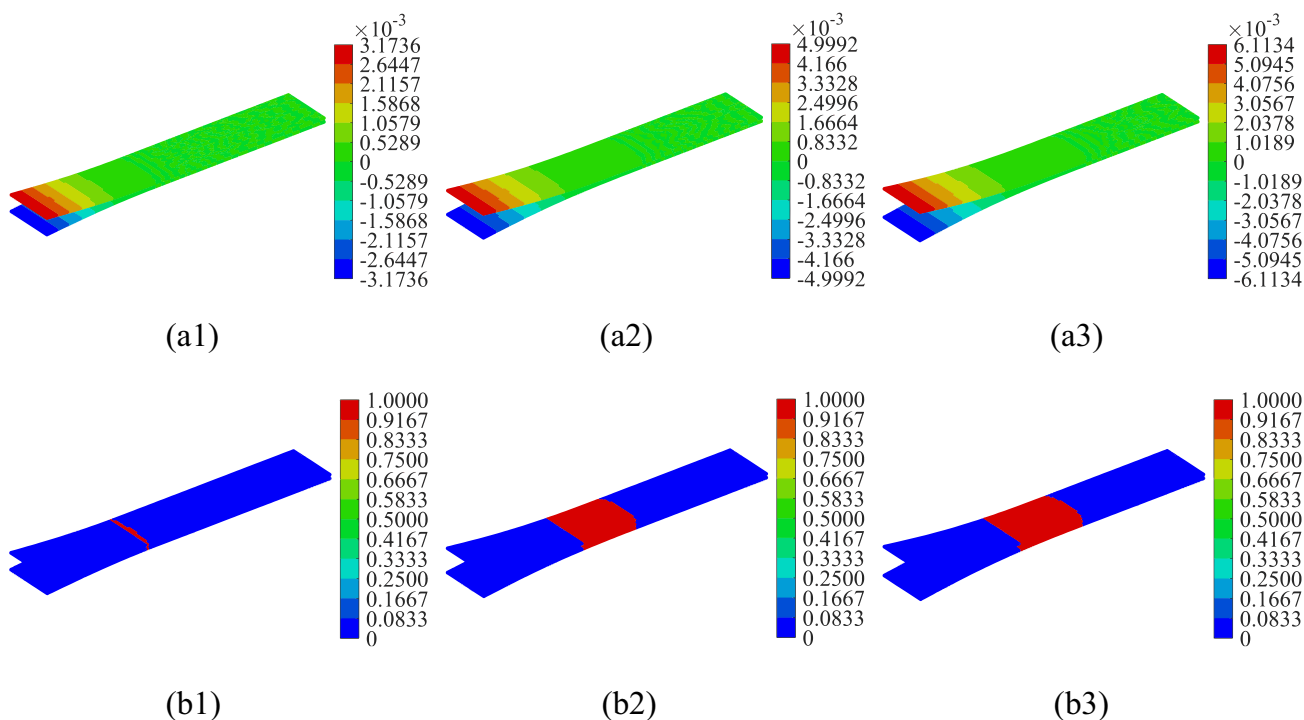


Fig. 22 The interlaminar damage of the DCB specimen corresponding z -direction displacement field when: (a1, b1) $w=3.17$ mm, (a2, b2) $w=4.99$ mm, (a3, b3) $w=6.11$ mm

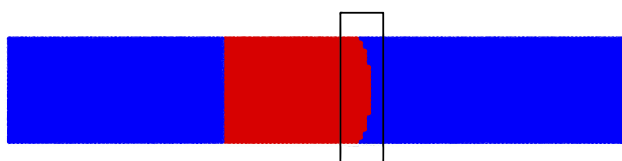


Fig. 23 Crack front profile of the DCB specimen

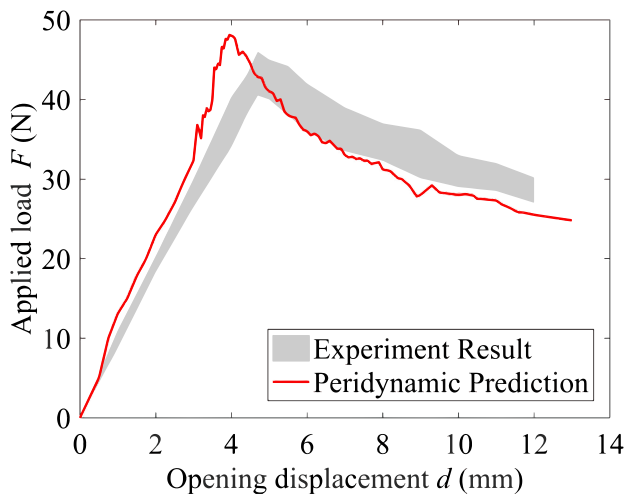


Fig. 24 Load–displacement curve of the DCB specimen

Figure 19 presents the experimental results of the laminate. It can be seen that the fiber breakage exists in the loading region, which is the main failure mode of the laminate. Also, matrix failure and interlaminar damage can also be observed near the loading region. Since the laminate is simulated only by a single layer of material points, both the interlaminar damage and the matrix damage are reflected as matrix damage in the numerical model. Obviously, the damage pattern predicted by the PD model is similar to the experimental observations.

The load is monitored by summing the forces between the interactions crossing this loading point. Figure 20 shows the comparison of experimental results and PD prediction of load–displacement relation. The predicted maximum load is $F_{max}=6778$ N, it is close to the experimental measurements of 6350 N. The relative error of the failure load is 6.31%, which demonstrates the capacity of the developed PD model to capture the damage pattern and failure load of the laminate.

The example demonstrates the capability of the proposed PD model in addressing damage initiation and its propagation for laminates, and an inherent theoretical advantage can be presented in characterizing discontinuities of materials. In addition, it can also be observed from this example that the stiffness degradation behavior of laminated structures can be described by means of the micromodulus reduction method.

5.4 DCB test

In this section, a challenging benchmark test of a Double Cantilever Beam (DCB) is simulated to validate the proposed PD model. The DCB specimen is composed of upper and lower arms, which are bonded with resin adhesive material. The dimensions of the laminate are $L \times B \times 2h = 150 \text{ mm} \times 25 \text{ mm} \times 3.66 \text{ mm}$, and there is a pre-existing crack with the initial length of $a_0 = 8 \text{ mm}$ in the middle of the laminate. The specimen is fixed on the right edges and subjected to a low rate of stretch along the left edges in both z and negative z directions, as illustrated in Fig. 21. The layup of the laminate is $[0]_{30}$, and the material parameters for the composite prepreg are: $E_{11} = 110 \text{ GPa}$, $E_{22} = 8.977 \text{ GPa}$, $G_{12} = 2.99 \text{ GPa}$, $\nu_{12} = 0.33$.

In PD simulations, the in-plane spacing between material points is $\Delta x = 1 \text{ mm}$, and the corresponding horizon size is $\delta = 3 \text{ mm}$. The laminate is uniformly discretized into two layers to characterize the upper and lower parts, and the numerical model contains a total of 7500 material points. To describe the mechanical behavior of the laminated structure, the out-of-plane bending and interlayer behavior of composite materials were considered in the PD analysis.

The bending behavior of the laminate is simulated by the proposed PD model, while the interlayer law is characterized by interlayer normal bonds and shear bonds proposed by Madenci and Oterkus [4]. Since the adhesive material exhibits a softening behavior, a bilinear constitutive is implemented in the interlayer bonds, which is defined as:

$$\sigma_I = \begin{cases} K_I \delta_I & \text{if } \delta_I \leq \delta_0 \\ S_I (\delta_f - \delta_I) / (\delta_f - \delta_0) & \text{if } \delta_I > \delta_0 \end{cases} \quad (76)$$

where δ_0 and δ_f represent the damage onset and ultimate opening displacement, respectively. Because the normal bond is similar to the cohesive model, its strength and stiffness parameters are $S_I = 9.5 \text{ MPa}$ and $K_I = 10^7 \text{ MPa/mm}$, respectively. The mode-I fracture energy of the adhesive material is $G_{IC} = 0.2 \text{ kJ/m}^2$.

Figure 22 presents the interlaminar damage evolution on the DCB specimen when the applied displacement is $w = 3.17 \text{ mm}$, 4.99 mm , and 6.11 mm , respectively. In

Fig. 22b1–b3, the blue regions represent the undamaged interface, and the adhesive interface is completely debonded in the red region. As shown in Fig. 22b1, the specimen initially gets damaged around the pre-existing crack tip when the applied displacement is $w = 3.17 \text{ mm}$. As the displacement increases, the DCB opens largely and the interlaminar damage propagates towards the right ends of the laminate, as shown in Fig. 22a3 and b3. Because the in-plane tension/compression behavior is not considered in this PD simulation, only normal bonds are utilized to constrain the relative separation of the DCB, and shear bonds do not participate in integration operations. Therefore, the damage coefficient of material points is only observed as 0 or 1.

Figure 23 shows the damage pattern in 2D view, and it is clearly seen that the crack front presents a curved profile. The reason for this physical phenomenon is that the two arms of the DCB behave as a plate structure, as discussed in [56], and the same crack shape was observed in the literature [57, 58]. The predicted load–displacement curve for this DCB is compared with the experimental results provided by Hu et al. [40], as shown in Fig. 24. The peak load predicted by developed PD is 48.1 N , which is close to the experimental measurements. Furthermore, it can also be seen that the trend of the curve is consistent with the experimental observations.

It can be seen from this example that the delamination damage pattern of the DCB can be well captured by combining the interlaminar law and the proposed PD model. Theoretically, other stiffness degradation behaviors can be further introduced into numerical models, such as exponential, polynomial, etc. In addition, it can also be observed that there is no need to introduce interlayer bonds between all adjacent plies, and only those interfaces that require attention are modeled. In a practical analysis, we should determine a reasonable modeling method according to the influence of the interface on the laminated structure, especially for a large-scale engineering structure.

6 Conclusion

In this study, a new peridynamic approach for predicting the bending and twisting mechanical behavior of laminated structures is proposed, in which two types of peridynamic

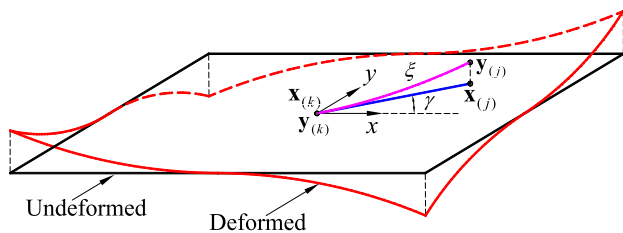


Fig. 25 Lamina subjected simple twisting

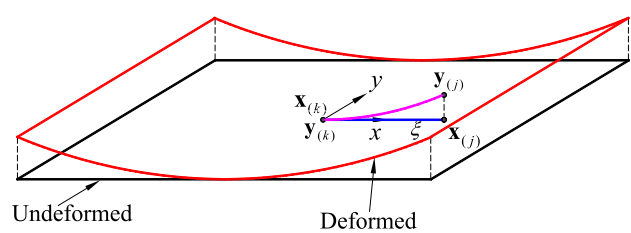


Fig. 26 Lamina subjected uniaxial bending in the fiber direction

bonds are utilized to account for the anisotropic properties of materials. Also, a single-layer material point model for laminates with a complex stacking sequence is implemented, and the computational efficiency can be significantly improved in comparison with multi-layer PD composite models. In addition, a micromodulus reduction method for describing the stiffness degradation behavior is also proposed for the first time in this paper. The accuracy of the proposed PD model is verified by comparing the FEA with PD results for composite laminates subjected to bending load. The damage predictions describe the general characteristics of experimentally observed failure mode well.

Since these flaws in the out-of-plane numerical theory of composite laminates and computational efficiency are overcome, deformation and damage problems of large composite structures can be analyzed by introducing coordinate transformation. Theoretically, the damage problem for any composite structures can be simulated, and PD theory can be expected to be applied to the real-scale composite structures. In addition, geometrically nonlinear relations can be further introduced into the the PD framework for large deformation analysis of laminated structures.

Appendix 1: PD material parameters

The geometric relationship between material points $\mathbf{x}_{(k)}$ and $\mathbf{x}_{(j)}$ can be obtained by Taylor expansion as:

$$\phi_{x(j)} = \phi_{x(k)} + \phi_{x,x(k)}(x_{(j)} - x_{(k)}) + \phi_{x,y(k)}(y_{(j)} - y_{(k)}) \quad (77a)$$

$$\phi_{y(j)} = \phi_{y(k)} + \phi_{y,x(k)}(x_{(j)} - x_{(k)}) + \phi_{y,y(k)}(y_{(j)} - y_{(k)}) \quad (77b)$$

where the higher-order terms of Taylor expansion are ignored, and the expressions in Eq. (77) can be further written as:

$$\frac{\phi_{x(j)} - \phi_{x(k)}}{\xi_{(j)(k)}} = \phi_{x,x(k)} \cos \gamma + \phi_{x,y(k)} \sin \gamma \quad (78a)$$

$$\frac{\phi_{y(j)} - \phi_{y(k)}}{\xi_{(j)(k)}} = \phi_{y,x(k)} \cos \gamma + \phi_{y,y(k)} \sin \gamma. \quad (78b)$$

Lamina subjected to simple twisting

For a lamina subjected to simple twisting, $\kappa_{12} = \kappa$, as shown in Fig. 25. The constitutive relation can be expressed as:

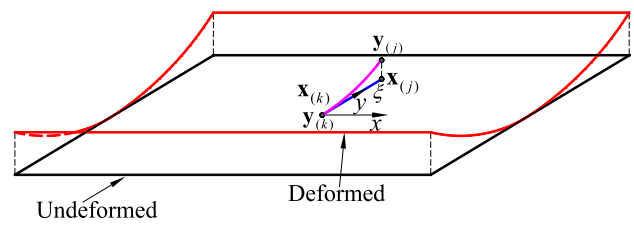


Fig. 27 Lamina subjected uniaxial bending in the transverse direction

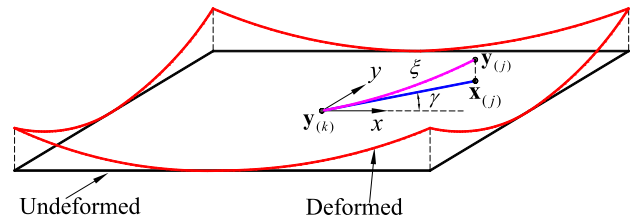


Fig. 28 Lamina subjected biaxial bending

$$\begin{Bmatrix} m_{11} \\ m_{22} \\ m_{12} \end{Bmatrix} = \begin{bmatrix} D_{11} & D_{12} & 0 \\ D_{12} & D_{22} & 0 \\ 0 & 0 & D_{66} \end{bmatrix} \begin{Bmatrix} 0 \\ 0 \\ \kappa \end{Bmatrix} \quad \text{or} \quad \begin{Bmatrix} m_{11} \\ m_{22} \\ m_{12} \end{Bmatrix} = \begin{Bmatrix} 0 \\ 0 \\ D_{66}\kappa \end{Bmatrix}. \quad (79)$$

The strain energy density based on CCM at material point $\mathbf{x}_{(k)}$ can be defined as:

$$W_{(k)} = \frac{1}{2} D_{66} \kappa^2. \quad (80)$$

The relative curvature between material points $\mathbf{x}_{(j)}$ and $\mathbf{x}_{(k)}$ in the deformed state can be expressed as:

$$\kappa_{(k)(j)} = \sin \gamma_{(j)(k)} \cos \gamma_{(j)(k)} \kappa. \quad (81)$$

The strain energy density can be calculated as:

$$W_{(k)} = c_{ft} \int_H \delta (\sin \gamma \cos \gamma \kappa)^2 \xi^2 dH \quad (82a)$$

or

$$W_{(k)} = c_{ft} h \int_0^\delta \int_0^{2\pi} \delta (\sin \gamma \cos \gamma \kappa)^2 \xi^2 d\xi d\phi = \frac{\pi h \delta^4 \kappa^2 c_{ft}}{12}. \quad (82b)$$

The PD strain energy density at material point $\mathbf{x}_{(k)}$ must be equal to the counterpart from CCM, Eqs. (80) and (82b), as follows

$$c_{ft} = \frac{6D_{66}}{\pi h \delta^4}. \tag{83}$$

Lamina subjected to uniaxial bending

For a lamina subjected to uniaxial bending in the fiber direction, $\kappa_{11} = \kappa$, $\kappa_{22} = 0$, as shown in Fig. 26. The constitutive relation can be expressed as:

$$\begin{Bmatrix} m_{11} \\ m_{22} \\ m_{12} \end{Bmatrix} = \begin{Bmatrix} D_{11}\kappa \\ D_{12}\kappa \\ 0 \end{Bmatrix} \tag{84}$$

where D_{11} and D_{12} represent the bending stiffness coefficients of orthotropic materials which can be expressed as:

$$[\mathbf{D}] = \begin{bmatrix} D_{11} & D_{12} & 0 \\ D_{12} & D_{22} & 0 \\ 0 & 0 & D_{66} \end{bmatrix} \tag{85}$$

where

$$D_{ij} = \frac{1}{12} q_{ij} t^3 \quad (i, j = 1, 2, 6). \tag{86}$$

The dilatation and strain energy density based on CCM at material point $\mathbf{x}_{(k)}$ can be defined as:

$$\theta_{(k)} = \kappa \quad W_{(k)} = \frac{1}{2} D_{11} \kappa^2. \tag{87a, b}$$

The relative curvature between material points $\mathbf{x}_{(j)}$ and $\mathbf{x}_{(k)}$ in the deformed state can be expressed as:

$$\kappa_{(k)(j)} = (\cos^2 \gamma_{(j)(k)}) \kappa. \tag{88}$$

Due to uniaxial bending deformation, the dilatation can be calculated as

$$\theta_{(k)} = d \int_H \delta(\cos^2 \gamma) \kappa dH \tag{89a}$$

or

$$\theta_{(k)} = \frac{\pi d h \delta^3 \kappa}{2}. \tag{89b}$$

The dilatation at material point $\mathbf{x}_{(k)}$ must be equal to the counterpart from CCM, Eqs. (87a) and (89b), as follows:

$$d = \frac{2}{\pi h \delta^3}. \tag{90}$$

The strain energy density of the lamina subjected to uniaxial bending can be calculated as:

$$W_{(k)} = a \kappa^2 + c_f \sum_{j=1}^J \delta(\cos^2 \gamma_{(k)(j)} \kappa)^2 \xi_{(k)(j)} V_{(j)} + c_{ft} \int_H \delta(\cos^2 \gamma \kappa)^2 \xi_{(k)(j)} dH \tag{91a}$$

or

$$W_{(k)} = a \kappa^2 + c_f \delta \kappa^2 \sum_{j=1}^J \xi_{(k)(j)} V_{(j)} + \frac{\pi h \delta^4 \kappa^2}{4} c_{ft}. \tag{91b}$$

Substituting Eq. (83) into Eq. (91b) and the integral value can be obtained as:

$$W_{(k)} = a \kappa^2 + c_f \delta \kappa^2 \sum_{j=1}^J \xi_{(k)(j)} V_{(j)} + \frac{3D_{66} \kappa^2}{2}. \tag{92}$$

The strain energy density at material point $\mathbf{x}_{(k)}$ must be equal to the counterpart from CCM, Eqs. (87b) and (92), as follows:

$$a + \delta \sum_{j=1}^J \xi_{(k)(j)} V_{(j)} c_f = \frac{1}{2} (D_{11} - 3D_{66}). \tag{93}$$

Similarly, for a lamina subjected to uniaxial bending in the transverse direction, $\kappa_{11} = 0$, $\kappa_{22} = \kappa$, as shown in Fig. 27. The expression can also be obtained as:

$$a + \delta \sum_{j=1}^J \xi_{(k)(j)} V_{(j)} c_t = \frac{1}{2} (D_{22} - 3D_{66}). \tag{94}$$

Lamina subjected to biaxial bending

For a lamina subjected to biaxial bending, $\kappa_{11} = \kappa$, $\kappa_{22} = \kappa$, as shown in Fig. 28. The constitutive relation can be expressed as:

$$\begin{Bmatrix} m_{11} \\ m_{22} \\ m_{12} \end{Bmatrix} = \begin{bmatrix} D_{11} & D_{12} & 0 \\ D_{12} & D_{22} & 0 \\ 0 & 0 & D_{66} \end{bmatrix} \begin{Bmatrix} \kappa \\ \kappa \\ 0 \end{Bmatrix} \quad \text{or} \quad \begin{Bmatrix} m_{11} \\ m_{22} \\ m_{12} \end{Bmatrix} = \begin{Bmatrix} (D_{11} + D_{12})\kappa \\ (D_{12} + D_{22})\kappa \\ 0 \end{Bmatrix}. \tag{95a, b}$$

The strain energy density based on CCM at material point $\mathbf{x}_{(k)}$ can be defined as:

$$W_{(k)} = \frac{1}{2} (D_{11} + 2D_{12} + D_{22}) \kappa^2. \tag{96}$$

The relative curvature between material points $\mathbf{x}_{(j)}$ and $\mathbf{x}_{(k)}$ in the deformed state can be expressed as:

$$\kappa_{(k)(j)} = (\cos^2 \gamma_{(j)(k)} + \sin^2 \gamma_{(j)(k)})\kappa. \tag{97}$$

The strain energy density of the lamina subjected to biaxial bending can be calculated as

$$W_{(k)} = 4a\kappa^2 + c_f\kappa^2\delta \sum_{j=1}^J \xi_{(k)(j)} V_{(j)} + c_{ft} \frac{2\pi h\delta^4 \kappa^2}{3} + c_t\kappa^2\delta \sum_{j=1}^J \xi_{(k)(j)} V_{(j)}. \tag{98}$$

Substituting Eq. (83) into Eq. (98) and the integral value can be obtained as:

$$W_{(k)} = 4a\kappa^2 + c_f\kappa^2\delta \sum_{j=1}^J \xi_{(k)(j)} V_{(j)} + 4D_{66}\kappa^2 + c_t\kappa^2\delta \sum_{j=1}^J \xi_{(k)(j)} V_{(j)}. \tag{99}$$

The strain energy density at material point $\mathbf{x}_{(k)}$ must be equal to the counterpart from CCM, Eqs. (96) and (99), as follows:

$$\begin{aligned} & \frac{1}{2}(D_{11} + 2D_{12} + D_{22} - 8D_{66}) \\ & = 4a + c_f\delta \sum_{j=1}^J \xi_{(k)(j)} V_{(j)} + c_t\delta \sum_{j=1}^J \xi_{(k)(j)} V_{(j)}. \end{aligned} \tag{100}$$

The PD material parameters of the lamina can be obtained by solving Eqs. (93–94) and (100), as:

$$\begin{aligned} a &= \frac{1}{2}(D_{12} - D_{66}) \\ c_f &= \frac{(D_{11} - D_{12} - 2D_{66})}{2\delta \sum_{j=1}^J \xi_{(k)(j)} V_{(j)}} \\ c_t &= \frac{(D_{22} - D_{12} - 2D_{66})}{2\delta \sum_{j=1}^J \xi_{(k)(j)} V_{(j)}}. \end{aligned} \tag{101}$$

In bond-based peridynamics (BBPD), the material parameter a associated with dilatation needs to vanish. Therefore, these elastic constants of lamina are limited as:

$$D_{12} = D_{66} \quad \text{and} \quad D_{22} = 3D_{12}. \tag{102}$$

The nonvanishing PD parameters, c_f and c_{ft} , can be presented as:

$$c_f = \frac{(D_{11} - D_{22})}{2\delta \sum_{j=1}^J \xi_{(k)(j)} V_{(j)}} \quad \text{and} \quad c_{ft} = \frac{6D_{66}}{\pi h\delta^4} \tag{103}$$

where c_f and c_{ft} represent the bending micromodulus of PD bonds in the fiber and arbitrary directions, respectively.

Appendix 2: Surface corrections

Similar to other PD models, the PD material parameters need to be corrected for those material points located in the boundary region. These correction factors can be determined by comparing the strain energy densities obtained from PD and CCM, and the corresponding moment–curvature relations can be modified.

When a lamina is subjected to constant curvature in the fiber and transverse direction, $\partial\theta_\alpha/\partial x_\alpha = \kappa$ with $(\alpha = 1, 2)$, the deformation field at material point \mathbf{x} can be described as:

$$\mathbf{u}_1^T(\mathbf{x}) = \left\{ \frac{\partial\theta_1}{\partial x_1} x_1 \quad 0 \right\} \quad \text{and} \quad \mathbf{u}_2^T(\mathbf{x}) = \left\{ 0 \quad \frac{\partial\theta_2}{\partial x_2} x_2 \right\}. \tag{104}$$

The PD strain energy density associated with $\mathbf{x}_{(k)}$ can be decomposed as:

$$W_\alpha^{\text{PD}}(\mathbf{x}_{(k)}) = W_{af}^{\text{PD}}(\mathbf{x}_{(k)}) + W_{aft}^{\text{PD}}(\mathbf{x}_{(k)}) \tag{105}$$

where W_{af}^{PD} and W_{aft}^{PD} represent strain energy densities of fiber bonds and matrix bonds, respectively. Each term in Eq. (105) can be calculated as:

$$W_{af}^{\text{PD}}(\mathbf{x}_{(k)}) = c_f\delta \sum_{j=1}^J \kappa_{(k)(j)}^2 V_{(j)} \tag{106a}$$

$$W_{aft}^{\text{PD}}(\mathbf{x}_{(k)}) = c_{ft}\delta \sum_{j=1}^\infty \kappa_{(k)(j)}^2 V_{(j)}. \tag{106b}$$

The corresponding strain energy density in CCM associated with material point $\mathbf{x}_{(k)}$ can also be defined as:

$$W_\alpha^{\text{CM}}(\mathbf{x}_{(k)}) = \frac{1}{2}D_{\alpha\alpha}\kappa^2 \quad (\alpha = 1, 2) \tag{107}$$

which can be decomposed as:

$$W_\alpha^{\text{CM}}(\mathbf{x}_{(k)}) = W_{af}^{\text{CM}}(\mathbf{x}_{(k)}) + W_{aft}^{\text{CM}}(\mathbf{x}_{(k)}) \tag{108}$$

where W_{af}^{CM} and W_{aft}^{CM} represent strain energy densities in the fiber direction and arbitrary directions, respectively.

For a lamina subjected to uniaxial bending in the fiber direction, each component of strain energy density can be expressed as:

$$W_{1f}^{\text{CM}}(\mathbf{x}_{(k)}) = \frac{1}{2}(D_{11} - D_{12} - 2D_{66})\kappa^2 \tag{109a}$$

$$W_{1ft}^{\text{CM}}(\mathbf{x}_{(k)}) = \frac{3}{2}D_{66}\kappa^2. \tag{109b}$$

For a lamina subjected to uniaxial bending in the transverse direction, each component of strain energy density can be expressed as:

$$W_{2f}^{CM}(\mathbf{x}_{(k)}) = 0 \quad (110a)$$

$$W_{2f}^{CM}(\mathbf{x}_{(k)}) = \frac{3}{2}D_{66}\kappa^2. \quad (110b)$$

Hence, for the uniaxial bending in the fiber direction, the correction factor components at material point $\mathbf{x}_{(k)}$ can be defined as:

$$S_{1f(k)} = \frac{W_{1f}^{CM}(\mathbf{x}_{(k)})}{W_{1f}^{PD}(\mathbf{x}_{(k)})} = \frac{\frac{1}{2}(D_{11} - D_{12} - 2D_{66})\kappa^2}{c_f \delta \sum_{j=1}^J \kappa_{(k)(j)}^2 V_{(j)}} \quad (111a)$$

$$S_{1ft(k)} = \frac{W_{1ft}^{CM}(\mathbf{x}_{(k)})}{W_{1ft}^{PD}(\mathbf{x}_{(k)})} = \frac{\frac{3}{2}D_{66}\kappa^2}{c_{ft} \delta \sum_{j=1}^{\infty} \kappa_{(k)(j)}^2 V_{(j)}}. \quad (111b)$$

When a lamina is subjected to uniaxial bending in the transverse direction, the correction factor components at material point $\mathbf{x}_{(k)}$ can be defined as:

$$S_{2f(k)} = 1 \quad (112a)$$

$$S_{2ft(k)} = \frac{W_{2ft}^{CM}(\mathbf{x}_{(k)})}{W_{2ft}^{PD}(\mathbf{x}_{(k)})} = \frac{\frac{3}{2}D_{66}\kappa^2}{c_{ft} \delta \sum_{j=1}^P \kappa_{(k)(j)}^2 V_{(j)}}. \quad (112b)$$

These correction factors in Eqs. (111–112) can be written in a vector form as:

$$g_{l(k)}(\mathbf{x}_{(k)}) = \{g_{1l}(\mathbf{x}_{(k)}), g_{2l}(\mathbf{x}_{(k)})\}^T = \{S_{1l(k)}, S_{2l(k)}\}^T \quad (l = f, ft). \quad (113)$$

Since these correction factors are only based on deformation in the fiber and transverse directions. To solve the correction factors in any direction, a unit relative position vector between material points $\mathbf{x}_{(k)}$ and $\mathbf{x}_{(j)}$ needs to be introduced, which can be expressed as:

$$\mathbf{n} = \frac{(\mathbf{x}_{(j)} - \mathbf{x}_{(k)})}{|\mathbf{x}_{(j)} - \mathbf{x}_{(k)}|} = \{n_1, n_2\}^T. \quad (114)$$

Therefore, the correction factor between material points $\mathbf{x}_{(k)}$ and $\mathbf{x}_{(j)}$ can be obtained as:

$$\bar{g}_{l(k)(j)} = \{\bar{g}_{l(k)(j)1}, \bar{g}_{l(k)(j)2}\}^T = \frac{\mathbf{g}_{l(k)} + \mathbf{g}_{l(j)}}{2}. \quad (115)$$

The total correction factor between material points $\mathbf{x}_{(k)}$ and $\mathbf{x}_{(j)}$ can be determined by projecting the correction factor components on the relative position vector as:

$$G_{l(k)(j)} = \left([n_1/\bar{g}_{l(k)(j)1}]^2 + [n_2/\bar{g}_{l(k)(j)2}]^2 \right)^{-1/2}. \quad (116)$$

Data availability The data are available upon reasonable request.

Declarations

Conflict of interest The authors declare no conflict of interest.

References

- Silling SA (2000) Reformulation of elasticity theory for discontinuities and long-range forces. *J Mech Phys Solids* 48:175–209
- Silling SA, Lehoucq RB (2010) Peridynamic theory of solid mechanics. *Adv Appl Mech* 44:73–168
- Silling SA, Askari E (2005) A meshfree method based on the peridynamic model of solid mechanics. *Comput Struct* 3:1526–1535
- Madenci E, Oterkus E (2014) *Peridynamic theory and its applications*. Springer, New York
- Bobaru F, Foster JT, Geubelle PH, Silling SA (2016) *Handbook of peridynamic modeling*. CRC Press, Boca Raton
- Gao C, Zhou Z, Li Z, Li L, Cheng S (2020) Peridynamics simulation of surrounding rock damage characteristics during tunnel excavation. *Tunn Undergr Space Technol* 97:103289
- Qin M, Yang D, Chen W, Yang S (2021) Hydraulic fracturing model of a layered rock mass based on peridynamics. *Eng Fract Mech* 258:108088
- Zhou Z, Li Z, Gao C, Zhang D, Bai S (2021) Peridynamic micro-elastoplastic constitutive model and its application in the failure analysis of rock masses. *Comput Geotech* 132(1):104037
- Yaghoobi A, Chorzepa MG (2017) Fracture analysis of fiber reinforced concrete structures in the micropolar peridynamic analysis framework. *Eng Fract Mech* 169:238–250
- Jin Y, Li L, Jia Y, Shao J, Burlion N (2021) Numerical study of shrinkage and heating induced cracking in concrete materials and influence of inclusion stiffness with Peridynamics method. *Comput Geotech* 133:103998
- Xu C, Yuan Y, Zhang Y, Xue Y (2021) Peridynamic modeling of prefabricated beams post-cast with steel fiber reinforced high-strength concrete. *Struct Concr* 22:445–456
- Zhang H, Qiao P (2018) An extended state-based peridynamic model for damage growth prediction of bimaterial structures under thermomechanical loading. *Eng Fract Mech* 189:81–97
- Zhang H, Zhang X, Liu Y, Qiao P (2022) Peridynamic modeling of elastic bimaterial interface fracture. *Comput Methods Appl Mech Eng* 390:114458
- Alebrahim R (2019) Peridynamic modeling of lamb wave propagation in bimaterial plates. *Compos Struct* 214:12–22
- Bathe K-J, Bolourchi S (1980) A geometric and material nonlinear plate and shell element. *Comput Struct* 11(1–2):23–48
- Bonet J, Wood RD (1997) *Nonlinear continuum mechanics for finite element analysis*. Cambridge University Press, Cambridge
- Hughes TJ, Pister KS, Taylor RL (1979) Implicit-explicit finite elements in nonlinear transient analysis. *Comput Methods Appl Mech Eng* 17:159–182
- Silling SA, Bobaru F (2005) Peridynamic modeling of membranes and fibers. *Int J Non Linear Mech* 40(2–3):395–409
- O’Grady J, Foster J (2014) Peridynamic plates and flat shells: a non-ordinary, state-based model. *Int J Solids Struct* 51(25–26):4572–4579

20. Diyaroglu C, Oterkus E, Oterkus S, Madenci E (2015) Peridynamics for bending of beams and plates with transverse shear deformation. *Int J Solids Struct* 69–70:152–168
21. Nguyen CT, Oterkus S (2019) Peridynamics for the thermomechanical behavior of shell structures. *Eng Fract Mech* 219:106623
22. Nguyen CT, Oterkus S (2020) Ordinary state-based peridynamic model for geometrically nonlinear analysis. *Eng Fract Mech* 224:106750
23. Nguyen CT, Oterkus S (2021) Ordinary state-based peridynamics for geometrically nonlinear analysis of plates. *Theor Appl Fract Mec* 112:102877
24. Shen G, Xia Y, Hu P, Zheng G (2021) Construction of peridynamic beam and shell models on the basis of the micro-beam bond obtained via interpolation method. *Eur J Mech-A/Solids* 86:104174
25. Oterkus E, Madenci E (2012) Peridynamic analysis of fiber-reinforced composite materials. *J Mech Mater Struct* 7(1):45–84
26. Hu W, Ha YD, Bobaru F (2012) Peridynamic model for dynamic fracture in unidirectional fiber-reinforced composites. *Comput Methods Appl Mech Eng* 217–220:247–261
27. Sun C, Huang Z (2016) Peridynamic simulation to impacting damage in composite laminate. *Compos Struct* 138:335–341
28. Hu YL, Yu Y, Wang H (2014) Peridynamic analytical method for progressive damage in notched composite laminates. *Compos Struct* 108:801–810
29. Hu YL, Carvalho N, Madenci E (2015) Peridynamic modeling of delamination growth in composite laminates. *Compos Struct* 132:610–620
30. Diyaroglu C, Madenci E, Phan N (2019) Peridynamic homogenization of microstructures with orthotropic constituents in a finite element framework. *Compos Struct* 227:111334
31. Diyaroglu C, Oterkus E et al (2016) Peridynamic modeling of composite laminates under explosive loading. *Compos Struct* 144:14–23
32. Silling SA, Epton M, Weckner O, Xu J, Askari E (2007) Peridynamic states and constitutive modeling. *J Elast* 88:151–184
33. Silling SA (2017) Stability of peridynamic correspondence material models and their particle discretizations. *Comput Methods Appl Mech Eng* 322:42–57
34. Gao Y, Oterkus S (2019) Fully coupled thermomechanical analysis of laminated composites by using ordinary state based peridynamic theory. *Compos Struct* 207:397–424
35. Gao Y, Oterkus S (2021) Coupled thermo-fluid-mechanical peridynamic model for analysing composite under fire scenarios. *Compos Struct* 255:113006
36. Hattori G, Trevelyan J, Coombs WM (2018) A non-ordinary state-based peridynamics framework for anisotropic materials. *Comput Methods Appl Mech Eng* 339:416–442
37. Fang G, Liu S et al (2021) A stable non-ordinary state-based peridynamic model for laminated composite materials. *Int J Numer Methods Eng* 122:403–430
38. Shang S, Qin XD, Li H et al (2019) An application of non-ordinary state-based peridynamics theory in cutting process modelling of unidirectional carbon fiber reinforced polymer material. *Compos Struct* 226:111194
39. Hu YL, Madenci E (2016) Bond-based peridynamic modeling of composite laminates with arbitrary fiber orientation and stacking sequence. *Compos Struct* 153:139–175
40. Hu YL, Yu Y, Madenci E (2020) Peridynamic modeling of composite laminates with material coupling and transverse shear deformation. *Compos Struct* 253:112760
41. Hu YL, Madenci E (2017) Peridynamics for fatigue life and residual strength prediction of composite laminates. *Compos Struct* 160:169–184
42. Jiang XW, Wang H (2018) Ordinary state-based peridynamics for open-hole tensile strength prediction of fiber-reinforced composite laminates. *J Mech Mater Struct* 13(1):53–82
43. Jiang XW, Wang H, Guo S (2019) Peridynamic open-hole tensile strength prediction of fiber-reinforced composite laminate using energy-based failure criteria. *Adv Mater Sci Eng* 2019:7694081
44. Guo J, Gao W et al (2019) Study of dynamic brittle fracture of composite lamina using a bond-based peridynamic lattice model. *Adv Mater Sci Eng* 2019:3748795
45. Braun M, Ariza MP (2019) New lattice models for dynamic fracture problems of anisotropic materials. *Compos Part B-Eng* 172:760–768
46. Braun M, Iváñez I, Ariza MP (2021) A numerical study of progressive damage in unidirectional composite materials using a 2D lattice model. *Eng Fract Mech* 249:107767
47. Braun M, Ariza MP (2020) A progressive damage based lattice model for dynamic fracture of composite materials. *Compos Sci Technol* 200:108335
48. Braun M, Aranda-Ruiz J, Fernández-Sáez J (2021) Mixed mode crack propagation in polymers using a discrete lattice method. *Polymers* 13(8):1290
49. Hu YL, Wang JY, Madenci E et al (2022) Peridynamic micromechanical model for damage mechanisms in composites. *Compos Struct* 301:116182
50. Buryachenko VA (2020) Generalized effective fields method in peridynamic micromechanics of random structure composites. *Int J Solids Struct* 202:765–786
51. Tastan A, Yolum U et al (2016) A 2D peridynamic model for failure analysis of orthotropic thin plates due to bending. *Procedia Struct Integr* 2:261–268
52. Ugur Y et al (2020) On the peridynamic formulation for an orthotropic Mindlin plate under bending. *Math Mech Solids* 25(2):263–287
53. Underwood PG (1983) Dynamic relaxation a review. In: *Computational Methods for Transient Dynamic Analysis*, vol 1. American Society of Mechanical Engineers, pp 245–265
54. Kilic B, Madenci E (2010) An adaptive dynamic relaxation method for quasi-static simulations using the peridynamic theory. *Theor Appl Fract Mech* 53(3):194–204
55. Qian Y (2018) Study on damage of laminates due to impact bending. Master's thesis, Southeast University
56. Zaccariotto M, Mudric T, Tomasi D et al (2018) Coupling of FEM meshes with Peridynamic grids. *Comput Methods Appl Mech Eng* 330:471–497
57. Budzik MK, Jumel J, Shanahan MER (2012) On the crack front curvature in bonded joints. *Theor Appl Fract Mech* 59(1):8–20
58. Jiang Z, Wan S, Zhong Z et al (2015) Effect of curved delamination front on mode-I fracture toughness of adhesively bonded joints. *Eng Fract Mech* 138:73–91

Publisher's Note Springer Nature remains neutral with regard to jurisdictional claims in published maps and institutional affiliations.

Springer Nature or its licensor (e.g. a society or other partner) holds exclusive rights to this article under a publishing agreement with the author(s) or other rightsholder(s); author self-archiving of the accepted manuscript version of this article is solely governed by the terms of such publishing agreement and applicable law.